Synthesis of tungsten oxide/ amino-functionalized sugarcane bagasse derived-carbon quantum dots (WO3/N-CQDs) composites for methylene blue removal

by Supandi Supandi

Submission date: 04-Nov-2021 11:19AM (UTC+0700)
Submission ID: 1692659524
File name: Chomospher_supandi.pdf (824.64K)
Word count: 8832
Character count: 46305

Chemosphere 277 (2021) 130300

Contents lists available at ScienceDirect

Chemosphere

journal homepage: www.elsevier.com/locate/chemosphere

Synthesis of tungsten oxide/ amino-functionalized sugarcane bagasse derived-carbon quantum dots (WO_3/N-CQDs) composites for methylene blue removal

Muhammad Wahyu Nugraha [a], Nur Hafizah Zainal Abidin [a], Supandi [b], Nonni Soraya Sambudi [a, c, *]

[a] Department of Chemical Engineering, Universiti Teknologi PETRONAS, Seri Iskandar, Perak, 32610, Malaysia
[b] Department of Pharmacy, Faculty of Pharmacy and Sciences, UHAMKA, Jakarta, 13460, Indonesia
[c] Centre of Urban Resource Sustainability (CUReS), Universiti Teknologi PETRONAS, Seri Iskandar, Perak, 32610, Malaysia

HIGHLIGHTS

- schematic approach for WO_3/amino-functionalized bagasse derived-carbon quantum dots (N-CQDs) composite preparation.
- The effects of EDA and EDTA amino-functionalized CQDs are observed.
- The pairing of N-CQDs into WO_3 refine to higher crystallinity, larger surface area, and quenched photo-luminescence intensity.
- The as-prepared WO_3/N-CQDs EDA 2.5% exhibits 96.86% methylene blue (MB) removal and good stability after 3 cycles.

GRAPHICAL ABSTRACT

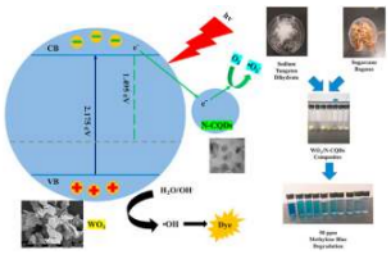

ARTICLE INFO

Article history:
Received 14 October 2020
Received in revised form
7 March 2021
Accepted 12 March 2021
Available online 18 March 2021

Handling Editor: Derek Muir

Keywords:
Amino-functionalized
Carbon quantum dots
Methylene blue degradation
Sugarcane bagasse
Tungsten oxide

ABSTRACT

In this present study, the tungsten oxide/amino-functionalized sugarcane bagasse derived-carbon quantum dots (WO_3/N-CQDs) composite has successfully been prepared through a simple mixing process. The WO_3 was synthesized through a precipitation method, and CQDs were amino-functionalized using ethylenedinitrilotetraacetic acid (EDTA) and ethylenediamine (EDA) through one-pot hydrothermal method. It is revealed that N-CQDs incorporation into WO_3 alters the bandgap energy, crystallinity, surface area, and photoluminescence (PL) properties. The produced composites exhibit higher monoclinic WO_3 crystallinity, larger surface area, lower bandgap energy and quenched photoluminescence intensity. The as-prepared WO_3/N-CQDs composites exhibit better adsorption and photocatalytic degradation performance of methylene blue (MB) than the pristine WO_3. It shows that the combination of N-CQDs and WO_3 enhanced visible light absorption, by lowering the bandgap energy of WO_3 from 2.175 to 1.495 eV. The best performance composite is WO_3/N-CQDs EDA 2.5% with an efficiency of 96.86%, removal rate constant of 0.02017/min, and chemical oxidation demand (COD) removal efficiency achieved 84.61%. Moreover, the WO_3/N-CQDs EDA 2.5% shows a significant photocatalytic activity even at higher MB initial concentration with 92.93% removal for 50 ppm MB. Subsequently, the composite also has good stability after a sequential 3-times cycle of degradation with 86.85% removal. The increasing photocatalytic performance is affected by the quenching effect of PL and lower bandgap energy. The

* Corresponding author. Department of Chemical Engineering, Universiti Teknologi PETRONAS, Seri Iskandar, Perak, 32610, Malaysia.
E-mail address: soraya.sambudi@utp.edu.my (N.S. Sambudi).

https://doi.org/10.1016/j.chemosphere.2021.130300

lower intensity of the PL indicates the reduced charge carrier recombination resulting in increased photocatalytic activity. The combination of N-CQDs and WO_3 resulted in improved photodegradation, which shows its significant potential to be utilized for wastewater treatment.

1. Introduction

The aquatic pollution from wastewater remains a crucial environmental issue until now. One of the hazardous effluents is dye, which vastly generated from numerous industries, such as textile, paper, petrochemical, and plastics, which contain more than 10,000 types of synthetic organic colorants (Zhang et al., 2017). The industrial effluent contains about 10–15% dyes (Mohammadi and Karimi, 2017). These effluents are rich in dyes, which some of the dyes are carcinogenic and dangerous to health and environment if they are not treated appropriately. In recent years, many treatment processes such as flocculation, chemical coagulation, simple sedimentation, aerated lagoons, aerobic activated sludge, trickling filters, reverse osmosis, photocatalytic oxidation, adsorption, and electrodialysis have been developed to treat wastewater (Liu et al., 2017; Mohammadi and Karimi, 2017). However, the adsorption process is desired as an environmentally friendly and cost-effective procedure. It has a high purification yield, and the choice of adsorbent plays an essential role in determining its cost efficiency (Elemen et al., 2012). On the other hand, the photocatalytic oxidation procedure was usually selected for its high yield, low energy use, simple process, mild reaction conditions, wide application range, and low secondary pollution (Zangeneh et al., 2015).

Heterogeneous photocatalysis has several advantages, such as it uses no reagent, and the only chemical used, metal oxide photocatalyst such as titanium dioxide (TiO_2), is abundant and harmless. However, TiO_2 photocatalysis has several drawbacks due to the high rate of recombination of electrons and holes and large bandgap energy, Eg of 3.0–3.2 eV (Xin et al., 2008), which can be only activated by UV light, that accounts for only 3–4% of the sunlight spectrum (Lewis, 2001). In contrast, visible light occupies 42–45% of the sunlight (Tian et al., 2015). Therefore, it is significant to develop a novel visible-light driven photocatalyst to efficiently increase solar light utilization. In the field of visible-light photocatalysis, many efforts such as doping (Sayed Abhudhahir and Kandasamy, 2015) and co-catalyst loading have been made (Prabhu et al., 2014).

One of the rising visible-light-driven photocatalysts is tungsten oxide (WO_3) due to its lower bandgap energy, nontoxicity, and resistance towards photo-corrosion (Su et al., 1997). However, its rapid recombination of photo-generated charge carriers limits the photocatalytic activity. Therefore, many modifications have been made to enhance the photocatalytic activity of WO_3 (Yan et al., 2016). Photoluminescent carbon quantum dots (CQDs) with sizes below 10 nm have been used as promising candidates for fluorescent materials in photocatalysis applications. The exceptional properties include a large two-photon absorption cross-section, low toxicity, and superior biocompatibility (Gu et al., 2016). The CQDs which have conjugated structure contributes to the excellent electron transfer/reservoir properties, that is the key factor in enhancing the photocatalytic activity (Zhang et al., 2016). Recently, numerous reports have proved that surface-modified carbon nanoparticles can absorb visible light to improve photocatalytic activity. Especially, photocatalysts doped by CQDs show much better catalytic (Ahmadi and Guinel, 2014). Thus, it is a great significance to investigate the particular photocatalytic application of CQDs.

Amino-functionalized nanostructured carbon materials can effectively prompt higher delocalized charge, lowering the work function of carbon, constructively enhance the photoluminescence (PL) emission performance and tune the electronic and optical properties of CQDs (Wu et al., 2014). Moreover, the usage of natural carbon precursors considering its low cost, environmentally friendly, and the underemployed such as sugarcane bagasse has been proved to be the suitable carbon source of CQDs. The fact that sugarcane bagasse has rich hydroxyl groups making it highly preferable for CQDs synthesis. Sugarcane is among the principal crops cultivated in tropical countries. The annual world production of sugarcane is ~1.6 billion tons, and it generates ~279 million metric tons (MMT) biomass residues (bagasse and leaves) (Chandel et al., 2012). Sugarcane bagasse (SB) has been explored in many applications such as activated carbons (ACs), carbon quantum dots (CQDs), and carbon nanotubes (CNTs), among others (Yahya et al., 2015; Zhang et al., 2016).

Until now, there are limited studies on the incorporation of N-CQDs into WO_3 as modified semi-conductors. Previous studies showed the extension of visible light absorption and remarkably reduced bandgap energy through the combination of N-CQDs/WO_3, which lead to a better photocatalytic performance attributed to enhanced charge separation efficiency for cyclohexane oxidation and methyl orange (MO) degradation (Jamila et al., 2020; Zhang et al., 2019). The unique properties and role of N-CQDs into semiconductors lead to the investigation of this study. However, the extensive processes and high energy of semi-conductor synthesis, as well as the usage of high-cost carbon precursors, hinder the improvement and the application of photocatalyst. Hence, in this study, sugarcane bagasse as a cheap and abundant biomass source is utilized as a precursor for CQDs.

In this work, the N-CQDs composite was prepared from sugarcane bagasse, functionalized with EDTA or EDA, and then combined with WO_3. The effect of different N-CQDs ratios incorporated into WO_3 for methylene blue (MB) photodegradation was evaluated. The as-prepared WO_3/N-CQDs exhibited lower bandgap energy, a higher degree of monoclinic crystallinity, larger surface area, and quenched PL. This study emphasizes the effect of quenched PL, which ultimately enhanced the photocatalytic performance of WO_3/N-CQDs even at high MB concentration that has not been explored before.

2. Material and methods

2.1. Materials

Sugarcane bagasse was obtained from a local market in Seri Iskandar, Perak, Malaysia. Sodium hydroxide pellets (CAS 1310-73-2), EDA (CAS 107-15-3), and Titriplex® III (EDTA) (CAS 6381-92-6) were purchased from Merck (Germany). Sodium tungstate dihydrate ≥99% (CAS 10213-10-2) was obtained from Sigma-Aldrich (USA), and hydrochloric acid (CAS 7647-01-0) was purchased from Fischer (USA). MB was purchased from Bendosen (Malaysia). These chemicals were employed without further purification or treatment. De-ionized (DI) water (18.2 MΩ) from PureLab Flex was

utilized for the whole experiment.

2.2. Synthesis of tungsten oxide

Tungsten oxide was synthesized via the precipitation method (Ahmadi and Guinel, 2014). First, 80 mL of hydrochloric acid (HCl) was added dropwise to 200 mL, 15 mM sodium tungstate dihydrate solution for 1 h. The solution was kept 5–10 °C, under constant stirring. Then, it was centrifuged and washed to reached pH ≈ 6 and then added 250 mL of deionized water, under constant stirring. The solution obtained was then ultrasonicated for 2 h before kept in room temperature for the crystallization process for 48 h. Then, the solution was vacuum filtered using a 0.45 μm PVDF membrane. WO_3 was dried at room temperature for 12 h.

2.3. Synthesis of amino-functionalized CQDs

The CQDs were synthesized from sugarcane bagasse using hydrothermal method, which has been published in the previous study (Liu et al., 2013) with modifications.

The CQDs were extracted from sugarcane bagasse. The sugarcane bagasse was prepared by cutting it into small pieces, and then the bagasse was washed with deionized water. The wet – pieces of sugarcane bagasse were dried in room temperature. Dried sugarcane bagasse was then burned in a muffle furnace at 600 °C for 1 h to obtain sugarcane bagasse biochar.

Following that, 300 mg of sugarcane bagasse biochar was added into sodium hydroxide 0.5 M 30 mL under constant stirring. Subsequently, the mixture was heated in a Teflon-lined stainless-steel autoclave for hydrothermal processes, which was done at temperature 190 °C for 24 h. Afterward, the solution was cooled to room temperature, and the carbon quantum dots (CQDs) solution was vacuum filtered by using a 0.45 μm PVDF membrane. The residue was dried separately at 60 °C. The CQDs solution was then dialyzed using a dialysis membrane (MWCO3500) overnight.

In this study, amino-functionalized CQDs were synthesized by following the same hydrothermal method as above. The sodium hydroxide, sugarcane bagasse biochar, and functionalization agent, EDA (2.5–10% v/v) or EDTA (1–3% w/w) were added and mixed under vigorous stirring for 2 h. After the hydrothermal process, the precipitated composite solution was vacuum filtrated. Afterward, the as-prepared N-CQDs solution was dialyzed for 24 h using dialysis membrane (MWCO3500).

2.4. Synthesis of tungsten oxide/amino-functionalized carbon quantum dots (WO_3/N-CQDs) composites

In this study, the heterojunction composites of WO_3/N-CQDs were prepared using liquid impregnation which have been previously performed in previous study (Jamila et al., 2020). The WO_3 sample was mixed with 1% amount of N-CQDs. Afterward, DI water was added into the solution to adjust the total volume of the mixture to 10 mL. The mixture was then magnetically stirred for 2 h. The samples were kept in an oven at 60 °C overnight until WO_3/N-CQDs composites in powder form were obtained.

2.5. WO_3/N-CQDs composites characterizations

The crystallinity of samples was recorded using an X-ray Diffractometer on X'Pert3 Powder and Empyrean PANalytical with Cu Kα irradiation (λ = 1.54) range (diffraction angles (2θ)) from 5 to 80 with a step size of 2 /step and exposure time of 1s/step. The sample functional groups were characterized using Fourier Transform Infrared Spectroscopy (FTIR) Perkin Elmer Spectrum One. The specific surface area was determined by BET analysis (Micromeritics Gemini 2375). PL spectra were recorded using Maya2000 Pro Spectrometer with 395 nm excitation wavelength, and UV–Visible spectra were analyzed using Cary Series UV–Vis Spectrophotometer. Next, X-Ray Photoelectron Spectrometer (XPS) analysis was conducted using Thermo Scientific K-Alpha. Zeiss Supra55 VP FESEM/EDX (Field Emission Scanning Electron Microscopy/Energy-dispersive X-ray) was used to investigate the samples morphology and composition. Imaging of samples was performed using High-Resolution Transmission Electron Microscope (HRTEM) 200 kV with Field Emission (Tecnai G2 20 S-Twin, FEI). The average particle sizes were determined using ImageJ software.

2.6. Photocatalytic study of WO_3/N-CQDs composites

The photocatalytic performance of WO_3/N-CQDs composites was measured by MB dye removal. The equipment set-up consists of a batch reactor equipped with a magnetic stirrer, 2 halogen lamps (each 80 W) (Philips, USA) as light source, and cooling fan. The cooling fan was used to maintain the surroundings temperature and prevent heating and evaporation of samples due to heat from light irradiation. The equipment was kept in the dark throughout the experiment to nullify the surrounding light effects and ensure that the removal of MB dye was only under the light source's irradiation. In each experiment, 0.6 g/L of composite WO_3/N-CQDs was dispersed into MB dye solution (5 ppm, 100 mL). Prior to turning on the lamp, the mixture of composite and MB dye was stirred vigorously and kept in the dark for 30min. At a certain time interval, 3 mL of sample was withdrawn and subsequently centrifuged to remove the remaining composite. The absorbance of samples was measured using UV–Vis spectrophotometer (Spectroquant Prove 600 (Merck, Germany), λ = 664.5 nm) to determine the MB dye concentration. Moreover, the chemical oxidation demand (COD) analysis was performed using DR3900 Spectrophotometer (HACH, USA). Firstly, the 2 mL of sample was added into the COD digestion solution (HACH, USA), then the solution was inverted to mix for 30 s. Following that, the solution heated in the COD reactor for 2 h at 150 °C. The solution was then cooled down to room temperature before the measurement of COD. The removal efficiency of MB dye can be expressed in the following Eq. (1):

$$\text{Removal Efficiency } (\%) = \frac{C_0 - C_e}{C_0} \times 100 \quad (1)$$

where C_0 and C_e are initial and remaining concentrations of MB dye, respectively.

3. Result and discussion

3.1. Morphology of WO_3/N-CQDs

The effect of different compositions of amino-functionalization upon the properties of CQDs is observed. The HRTEM imaging and size distribution (Fig. 1) show well-dispersed and spherical shape carbon dots with narrow size distribution. The size of N-CQDs EDTA 2% is 4.611 ± 0.727 nm in diameter calculated by measuring the diameter of 50 particles with around 0.207 nm lattice spacing. Comparing with N-CQDs EDTA 3%, the diameter decreases to approximately 4.197 ± 1.058 nm with 0.209 nm lattice spacing. On the other hand, both N-CQDs EDA 5% and 10% have higher diameter range than the EDTA as mentioned above, at around 9.704 ± 1.428 nm with 0.202 nm lattice spacing and 8.898 ± 2.018 nm 0.310 nm lattice spacing, respectively. Thus, the amino-functionalization can alter the CQDs size by edge-termination at higher amine concentrations, similarly seen in the

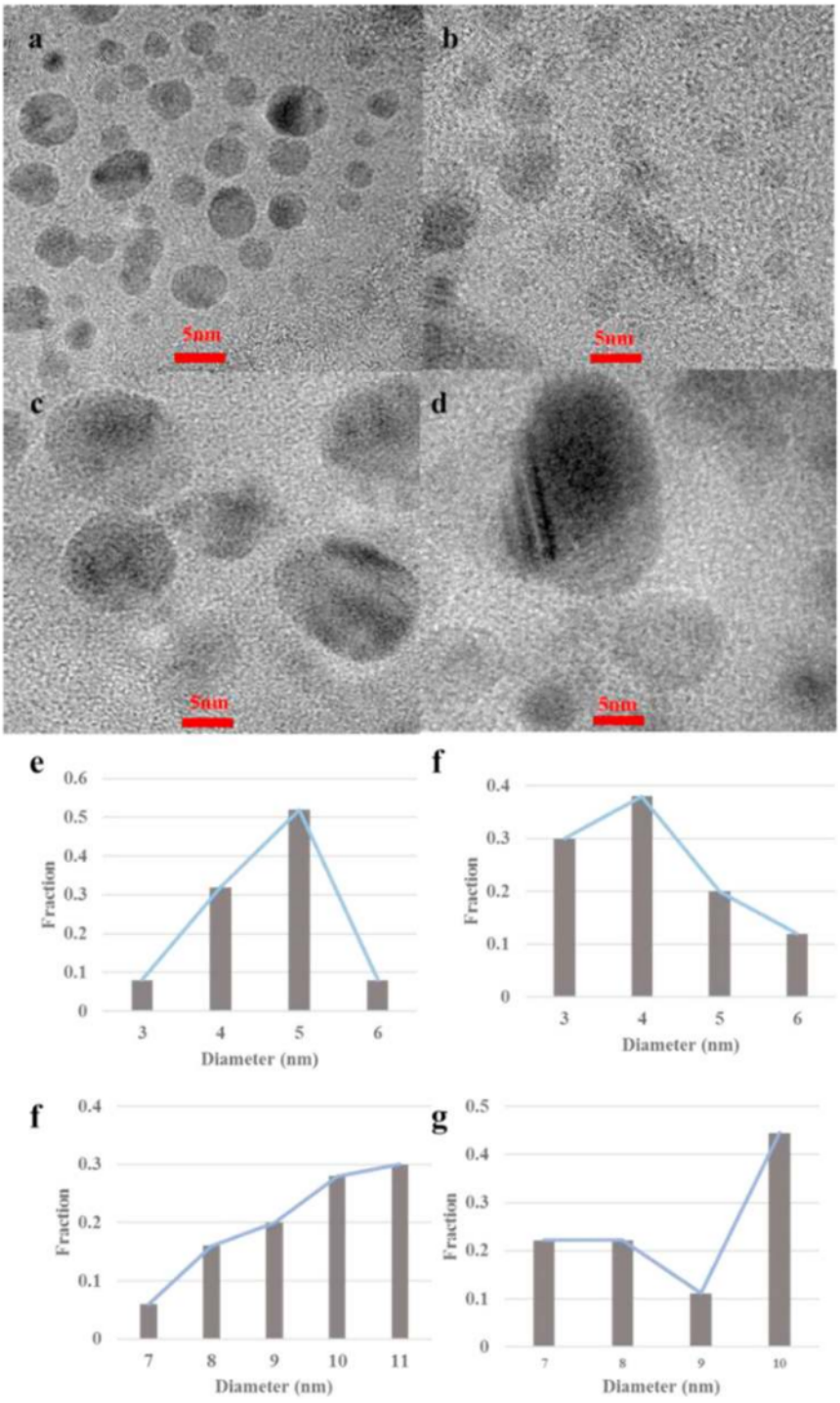

Fig. 1. HRTEM images of (a) N-CQDs EDTA 2%, (b) N-CQDs EDTA 3% (c) N-CQDs EDA 5% (d) N-CQDs EDA 10%, Size distribution (e) N-CQDs EDTA 2%, (f) N-CQDs EDTA 3% (g) N-CQDs EDA 5% (h) N-CQDs EDA 10%.

previous study (Tetsuka et al., 2012).

Secondly, Fig. 2 presents the FESEM images of WO_3 and WO_3/N-CQDs composite. Fig. 2 (a) shows pristine WO_3 with 2D sheet-like building blocks with a length of 200–300 nm. Close observation in Fig. 2 (b) reveals the sheet possesses a thickness of 20–50 nm. Moreover, the WO_3 sample decorated with N-CQDs maintain the same nanosheet structure. The HRTEM images of WO_3/N-CQDs EDA 2.5% in Fig. 3 shows that the nanosheet structure has high degree of crystallinity with a lattice spacing of 0.202 nm.

Furthermore, the surface area of the selected composites was also analyzed. The addition of 2.5% N-CQDs EDA was found to increase the surface area of WO_3 (Table 1). However, the specific surface area of the composite decreases after further increasing N-CQDs loading, which can be seen for WO_3/N-CQDs EDA 2.5% and WO_3/N-CQDs EDA 10%. This can be attributed to the pore blockage where the amino-functionalized CQDs occupy the empty porous space of organic linkers at higher loading (Horiuchi et al., 2012; Wang et al., 2015). In general, the large surface area provides more available active sites for photocatalytic reactions (Horiuchi et al., 2012).

3.2. Functional groups of WO_3/N-CQDs

The functional groups of samples are identified using FTIR

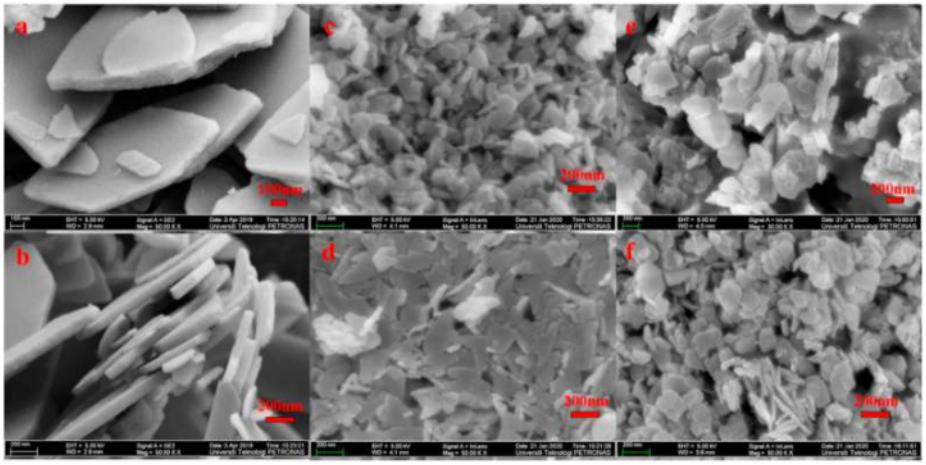

Fig. 2. FESEM images of (a) (b) pure WO_3, (c) WO_3/N-CQDs EDTA 1%, (d) WO_3/N-CQDs EDTA 3%, (e) WO_3/N-CQDs EDA 2.5%, and (f) WO_3/N-CQDs EDA 10%.

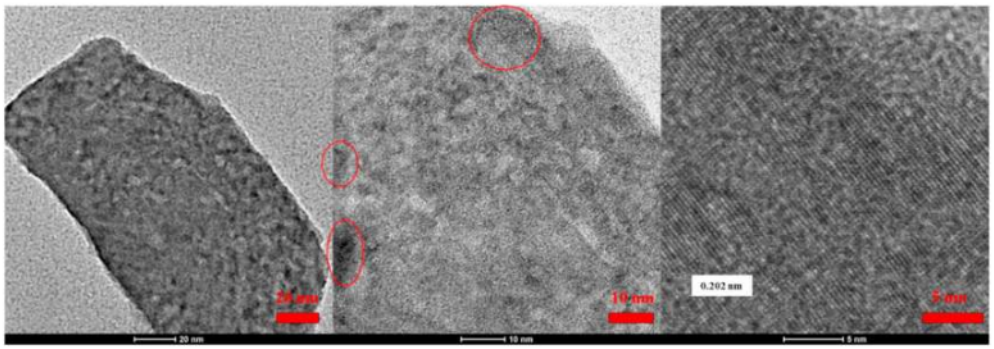

Fig. 3. HRTEM images of WO_3/N-CQDs EDA 2.5%.

Table 1
The surface area of selected composite.

Sample	Surface Area (m^2/g)	Pore Size (nm)	Total Pore Volume (cm^3/g)
Pure WO_3	7.5	6.245	0.0117
WO_3/N-CQDs EDTA 3%	19.9	25.772	0.1288
WO_3/N-CQDs EDA 2.5%	25.3	29.106	0.1841
WO_3/N-CQDs EDA 10%	19.2	24.576	0.1181

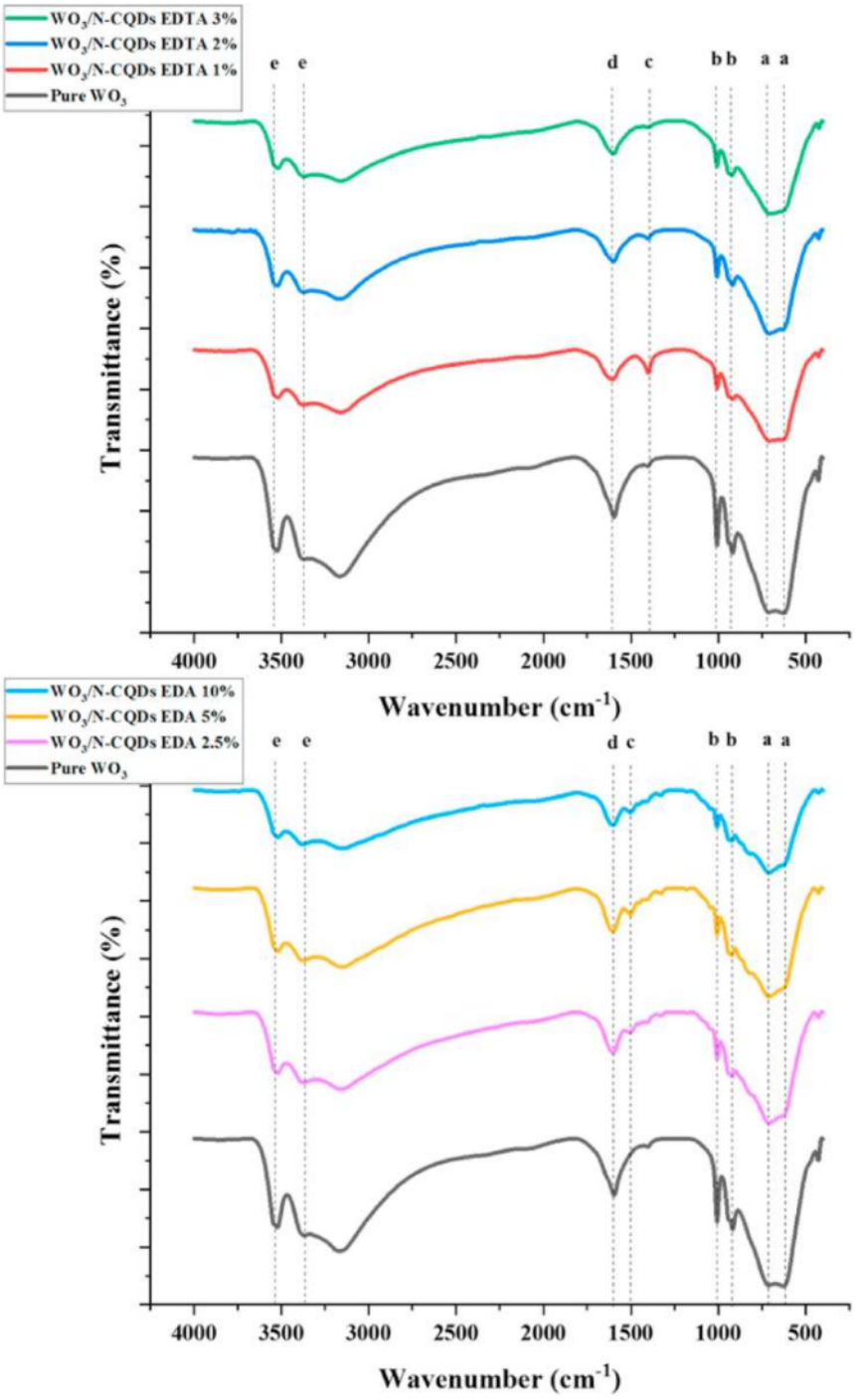

Fig. 4. FTIR spectra of WO_3/N-CQDs composites.

Table 2
EDX elemental composition of WO_3/N-CQDs samples.

Sample		Element			
		W	O	C	N
Pristine WO_3	Weight %	65.03	34.97	–	–
	Atomic %	21.74	78.26	–	–
WO_3/N-CQDs EDTA 1%	Weight %	55.72	35.04	9.23	–
	Atomic %	11.23	66.91	21.87	–
WO_3/N-CQDs EDTA 2%	Weight %	67.57	26.35	6.09	–
	Atomic %	15.00	65.26	19.74	–
WO_3/N-CQDs EDTA 3%	Weight %	59.13	24.06	16.82	–
	Atomic %	9.97	46.62	43.41	–
WO_3/N-CQDs EDA 2.5%	Weight %	65.01	28.85	6.14	–
	Atomic %	13.25	67.60	19.15	–
WO_3/N-CQDs EDA 5%	Weight %	64.81	26.17	9.02	–
	Atomic %	12.87	59.72	27.41	–
WO_3/N-CQDs EDA 10%	Weight %	60.57	25.9	13.52	–
	Atomic %	10.93	52.74	36.32	–

tra (Fig. 4). The characterization was performed to determi functional groups after the addition of functionalized N-CQDs on the surface of tungsten oxide. The peaks at 626 and 710 cm^{-1} (peaks a) are attributed to W–O stretching mode, while peaks at 917 and 1006 cm^{-1} (peaks b) are assigned to W=O bond which confirms the generation of tungsten oxide nanostructures (Zhan et al., 2018). The characteristic peaks of N-CQDs can be seen m the bending vibration of N–H at 1500 cm^{-1} (peak c) (Liu et al., 2016; Madrakian et al., 2017; Nogueira et al., 2013) while the peak slightly shifted to the right in WO_3/NCQDs EDTA. The increasing amount of amino-functionalization agents indicates a higher peak response in both EDTA and EDA. Subsequently, the narrow bending at 1640 cm^{-1} (peak d) is the characteristic of H–O–H of the water molecule (Doma et al., 2020), and the broad k at 3403 cm^{-1} (peak e) is indicated for O–H bending vibration on the surface of WO_3/N-CQDs (Ţucureanu et al., 2016). This is attributed to the N-CQDs that is rich in oxygen-containing groups and the uniform bonding of carbon dots and semiconductors, both indicate the good dispersion of N-CQDs (Li et al., 2012). Therefore, WO_3/N-CQDs composites are bound by different groups interactions.

3.3. Energy dispersive X-ray analysis

The EDX analysis was performed to identify the elemental composition of the synthesized samples. The spectrum, re-sented in Table 2 confirms that pristine WO_3 is composed of W and O elements without any impurities. On the other hand, the composites WO_3/N-CQDs exhibit W, O, and C elements, which indicates the N-CQDs are exist on the surface of WO_3. However, EDX did not detect any N element. This can happen due to the selected area contains too little nitrogen dopants to be measured (Sial et al., 2020). Nevertheless, the evidence of nitrogen in the composites is determined using XPS analysis.

3.4. X-ray photoelectron spectroscopy analysis of WO_3/N-CQDs sample

The elemental analysis of the WO_3/N-CQDs sample was carried out to further confirm the amino-functionalized CQDs existence in WO_3. The full scan of X-ray photoelectron spectroscopy spectra shown in Fig. 5 reveal certain p s at binding energy of 47.98, 297.98, 409.98, 544.98 eV, which correspond to W4f, C1s, N1s, and O1s, respectively. Furthermore, the bulk analyses indicate that the WO_3/N-CQDs sample contained element of W 20.12, O 56.91, C 16.88, N 6.08 wt%, respectively. Additionally, the high-resolution spectra of W4f exhibit peaks centered at 38.16, 39.71, and 41.71 eV ributed to $W4f_{5/2}$, $W4f_{5/2}$, and $W5p_{3/2}$, respectively (Ahmadi et al., 2014; Huang et al., 2019; Shi et al., 2016). Secondly, the C1s high-resolution spectra reveal deconvoluted two peaks centered at 288.77 and 290 eV assigned to C–O/C–N and C=O, respectively (Zhang et al., 2019). Thirdly, N1s spectra consist of the 3 peaks centered at 401.13, 403.96, and 405.58 eV belong to the binding energy of $N–C_3$ (tertiary amine), N–H, and CNH_2 (primary amine) (Huang et al., 2020). Lastly, the O1s high-resolution spectra fitted into two peaks centered at 533.35 and 533.88 correspond to C–O and W–O/WO = , respectively (Huang et al., 2019; Shi et al., 2016).

3.5. Crystallinity of WO_3/N-CQDs

The XRD spectra (Fig. 6) of prepared WO_3 nanosheets and WO_3/N-CQDs composite show the combination of diffraction peaks of WO_3 monoclinic phase (JCPDS No. 18–1420) and WO_3 cubic phase (JCPDS No. 054–0508). The monoclinic peaks clearly exhibited at 11.1°, 23.7°, 24.2°, 34°. Meanwhile, a peak at 25.9° is ascribed to the cubic phase. It is shown that the loading of N-CQDs changes the crystalline structure of WO_3 significantly to monoclinic structure as the results of the interaction between carbon dots and WO_3. Subsequently, the other strong peaks at 10,3°, 17.1°, 27.1°, and 35.5°are consistent with the diffraction peak of ammonium tungsten oxide (JCPDS No. 25–0045), which can be attributed to the interaction between $–NH_2$ in NCQDs and WO_3 to form ammonium tungsten oxide on the composite surface (Zhang et al., 2019). Evidently, the increase of the amino-functionalization on the NCQDs increases the peaks mentioned earlier. Besides, the peak at 29.6° is observed as the amorphous nature of carbon, and the region ranging between 20° and 40° represents the different functional groups of ternary composites (Jamila et al., 2020). On the contrary, no broad diffraction peaks of carbon dots were observed due to their low content and low diffraction intensity (Zhang et al., 2016).

3.6. UV–Vis DRS of WO_3/N-CQDs

The UV–Vis absorption spectra were analyzed to study the role of N-CQDs. The absorption of WO_3 and WO_3/N-CQDs composites were analyzed using UV–vis D and summarized in Fig. 7. The pure WO_3 nanosheets show no absorption in the region of 500–700 nm which corresponds to the intrinsic absorption property of pristine W (Zhang et al., 2019). The WO_3/N-CQDs composite exhibits strong absorption in the UV light region and significantly enhanced the visible light region's absorption at

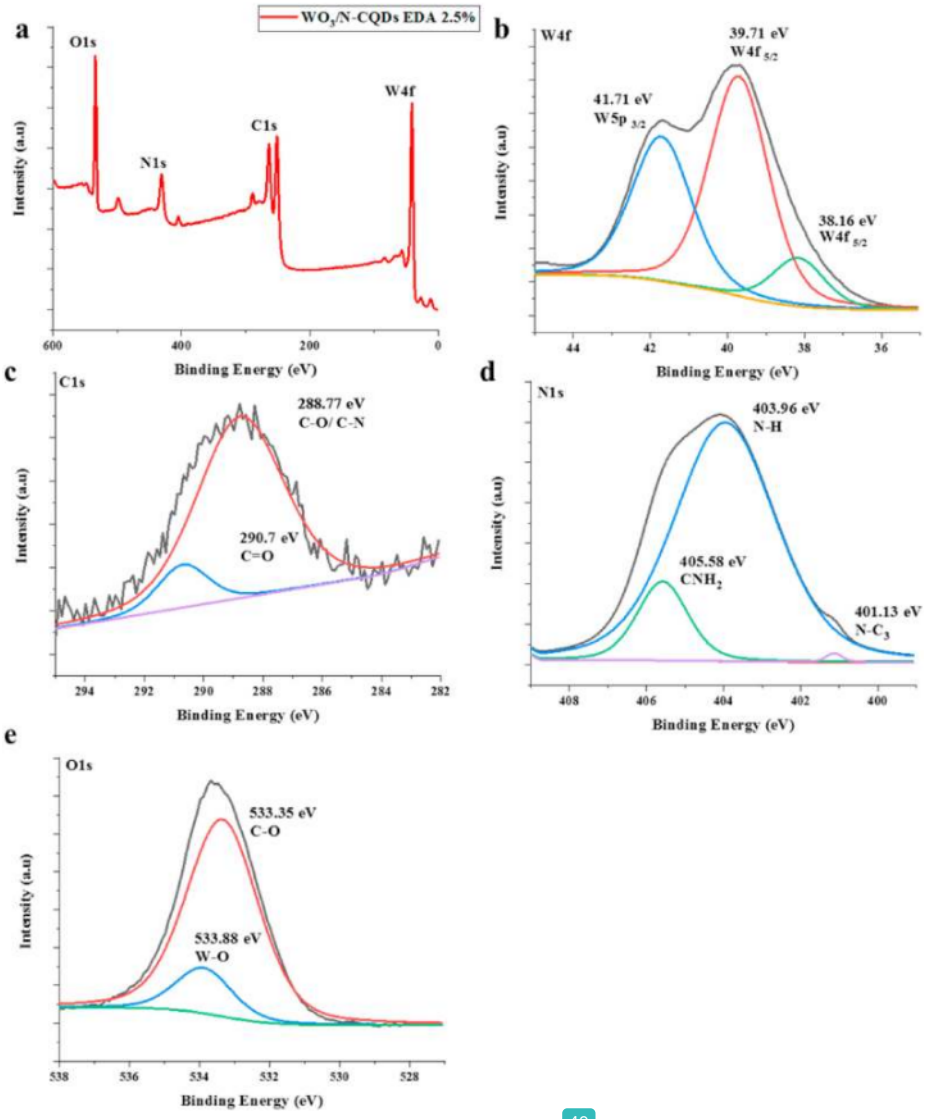

Fig. 5. XPS spectra of WO_3/N-CQDs EDA 2.5% (a) full spectra, high-resolution (b) W4f spectra, (c) C1s spectra, (d) N1s spectra, (e) O1s spectra.

380–700 nm. This indicates that the loading of N-CQDs can effectively improve the absorption capacity of WO_3 nanosheets in the visible light region (Song et al., 2017; Zhang et al., 2019). Moreover, it is clearly illustrated that the increasing amount of amino-functionalization agents in NCQDs lowers the absorption intensity. The overdose effect of N-doped in NCQDs tends to make them aggregate together to form larger particles (>10 nm), resulting in weak visible light absorption (Zhang et al., 2016).

Furthermore, the estimated bandgap energy of each WO_3/N-CQDs composite is also calculated. The bandgap energy values of pure WO3, WO_3/N-CQDs EDTA 1%, WO_3/N-CQDs EDTA 2%, WO_3/N-CQDs EDTA 3%, are 2.175, 1.925, 1.975, 2 eV, respectively. While the bandgap energy values of WO_3/N-CQDs EDA 2.5%, WO_3/N-CQDs EDA 5%, and WO_3/N-CQDs EDA 10% are 1.495, 1.5, and 1.8 eV, respectively. This corresponds to the overdose effect of the N-doped in NCQDs. Evidently, the WO_3/N-CQDs composite has better performance for harvesting light in the visible light region (1.7–3.1 eV).

3.7. Optical properties of WO_3/N-CQDs

Fig. 8 illustrates the photoluminescence properties of WO_3/N-CQDs at different concentrations. The optical properties of WO_3/N-CQDs were observed using PL photoluminescence spectroscopy with excitation wavelength at 350 nm. The emission peak observable at 590–610 nm with the center peak at 605 nm. It can be seen clearly that the PL intensity of WO_3/N-CQDs is remarkably quenched with addition of NCQDs. Firstly, at the lower amount of N-CQDs, the PL intensity is quenched at the highest rate. The increasing amount of N-CQDs lowers the quenching effect of the PL intensity. This might be due to the overdose effect that is

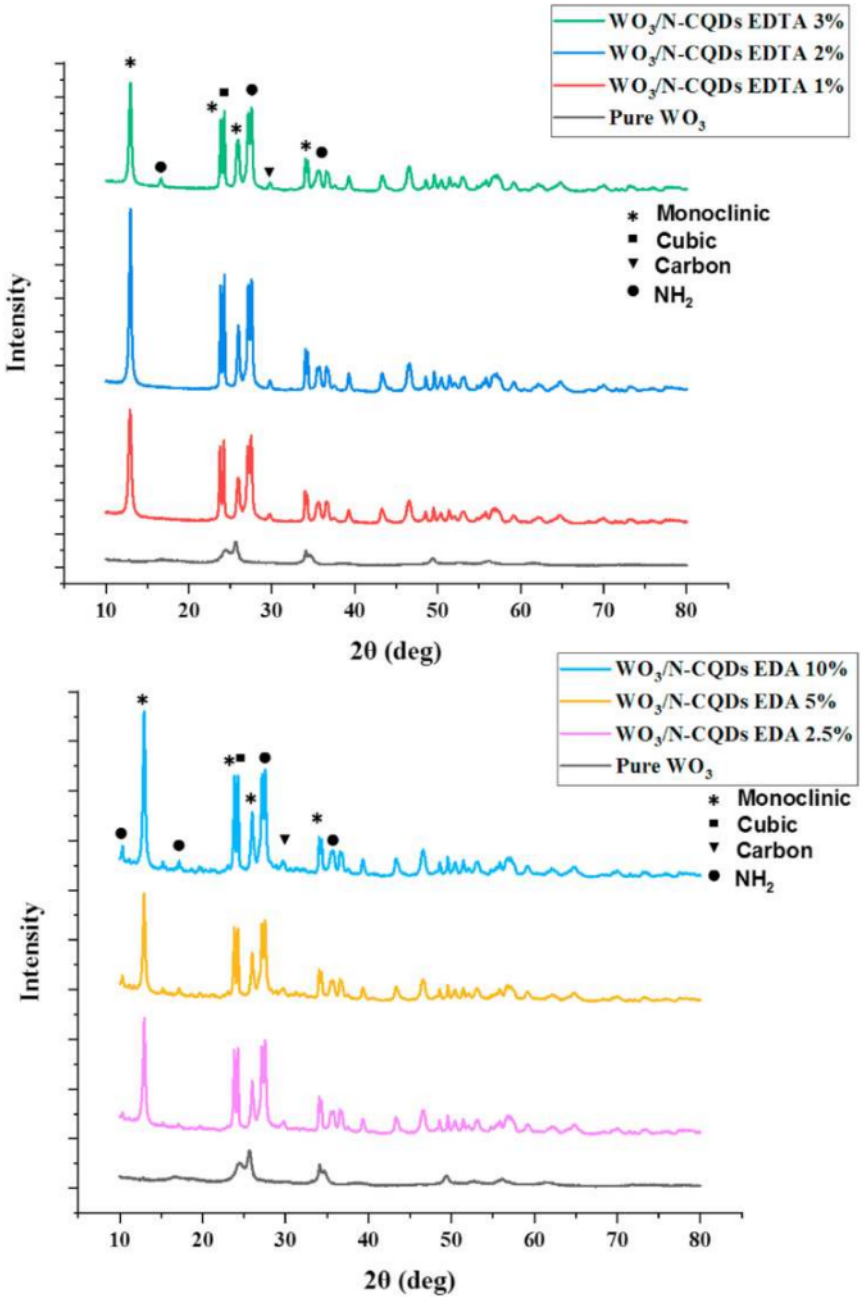

Fig. 6. XRD spectra of WO_3/N-CQDs samples.

mentioned earlier. The overdose effect tends to form aggregate to arrange larger particles structure (Zhang et al., 2016). The PL's lower intensity indicates reduced charge carrier recombination, which is caused by photons emission from the electron-hole pair recombination (Jamila et al., 2020). The addition of nitrogen in CQDs corresponds to the enhanced quantum excessiveness of synthesized photocatalysts and then effectively allocated the generated electrons from the surface of WO_3 (Ching Sim et al., 2018). Consequently, the reduction of charge carrier recombination resulting in increased photocatalytic activity (Fig. 9).

3.8. Photocatalytic performance of WO_3/N-CQDs

The performance of WO_3/N-CQDs in the photocatalytic

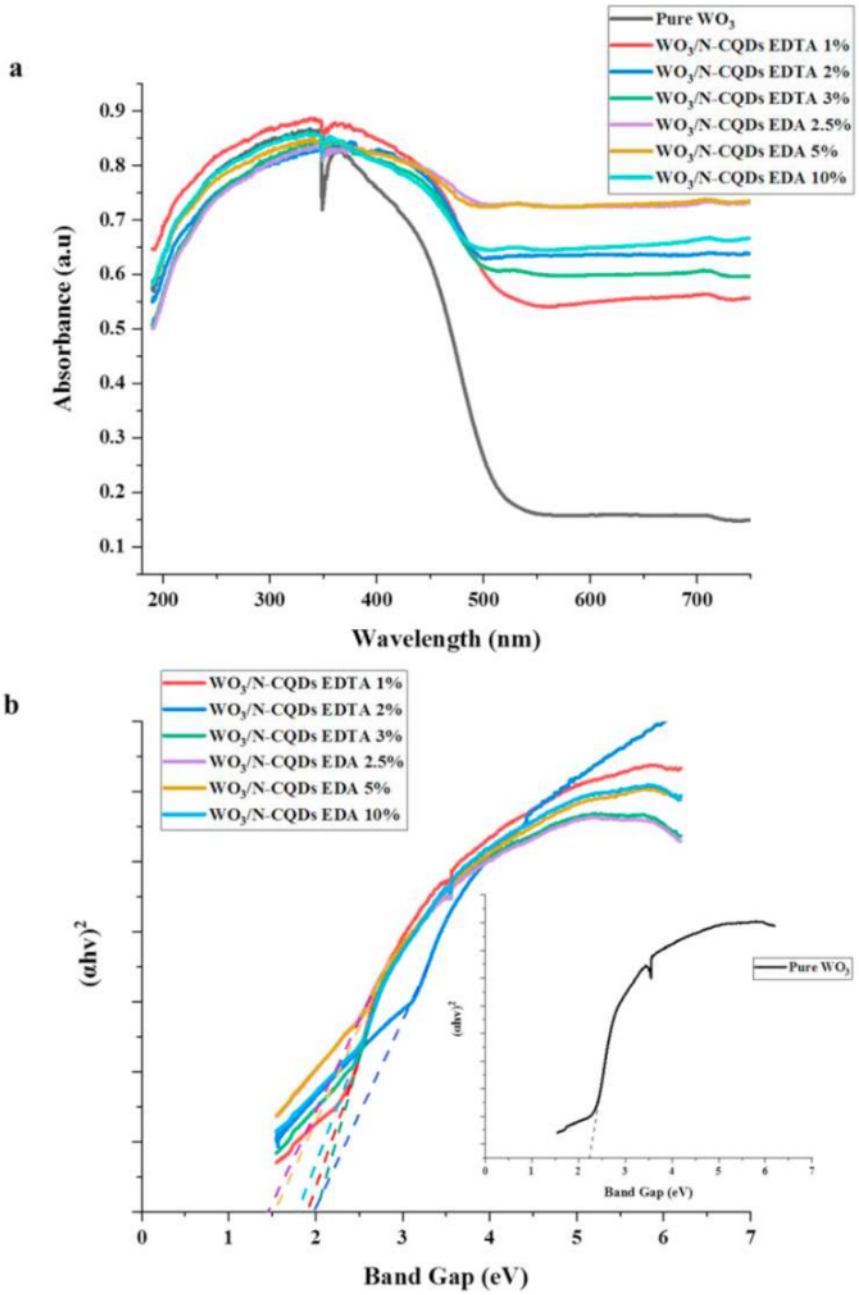

Fig. 7. (a) UV–Vis absorption spectra of WO_3/N-CQDs, and (b) Bandgap energy of WO_3/N-CQDs samples with an inset of bandgap energy of pure WO_3.

application is observed using MB dye removal. The preliminary investigation of self-removal MB towards visible irradiation light is performed, where MB solution in the absence of WO_3/N-CQDs was irradiated, and this was depicted as blank. The result shows that the visible light irradiation slightly degrades the MB, which indicates that the self-removal of MB dye contributes to the performance of WO_3/N-CQDs in the range of 9–10%. Furthermore, the adsorption of WO_3 is also investigated, in which MB is mixed alongside pure WO_3 without any visible light irradiation. It is shown that tungsten oxide has apparent adsorption performance by removing MB up to 90%. Compared to the pure WO_3 with visible light irradiation, the MB removal is slightly increased. The similar high adsorption behavior of WO_3 composite can be seen from previous studies. Liu et al., successfully prepared $SrTiO_3$(La,Cr)-decorated WO_3 nanosheets with 55% removal using 15 ppm MB (Liu et al., 2017). Comparably, Shang et al., achieved 71.5% adsorption efficiency of 40 ppm MB

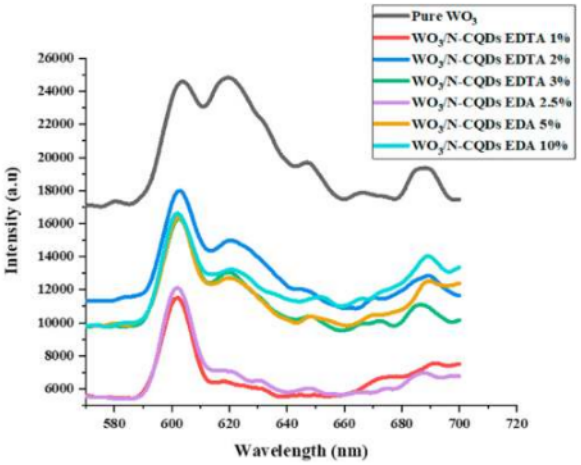

Fig. 8. Photoluminescence spectra of WO_3/N-CQDs.

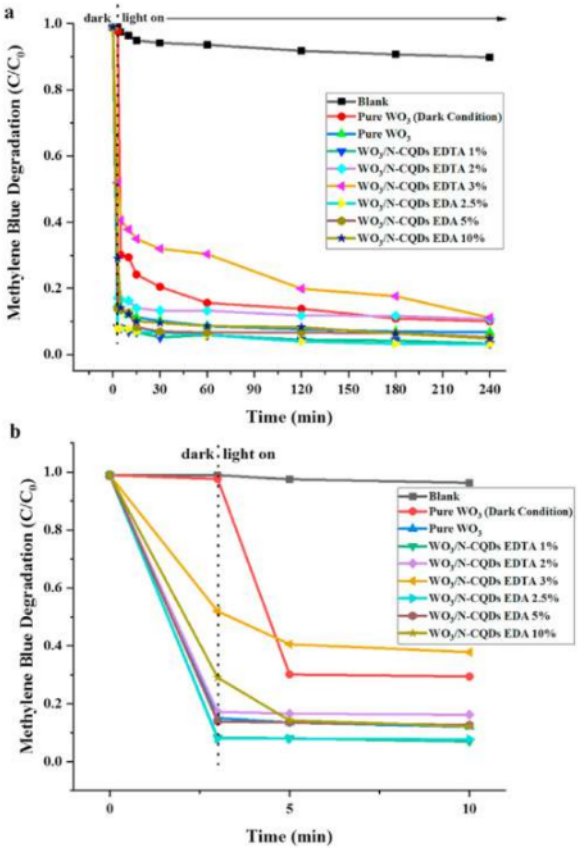

Fig. 9. (a) Photocatalytic performance of WO_3/N-CQDs composites under visible light irradiation by removing 5 ppm of MB dye (b) Inset photocatalytic performance at 0–10 min.

using $W_{18}O_{49}$ composite (Shang et al., 2020).

Moreover, the performance of composite WO3/N-CQDs is observed. The result exhibits that the N-CQDs enhanced the adsorption and photocatalytic performance of WO_3. The adsorption rate can be observed during the dark experiment within 30 min prior to the light switched on, where only the adsorption process took place. Both composites of WO_3 with the lowest amino-functionalization N-CQDs EDTA 1% and EDA 2.5% have the best adsorption performance compared to higher amino-functionalization of N-CQDs.

The photocatalytic performance was observed after the light source was switched on, where the photocatalytic reaction performed. The MB removal increases in the order of pure WO_3, followed by WO_3/N-CQDs EDTA 3%; WO_3/N-CQDs EDTA 2%, WO_3/N-CQDs EDTA 1%, and WO_3/N-CQDs EDA 10%, WO_3/N-CQDs EDA 5%, WO_3/N-CQDs EDA 2.5%, respectively. The highest removal found in WO_3/N-CQDs EDA 2.5% with 96.86% removal efficiency. The higher photocatalytic activity occurred at initial N-CQDs concentration, but it decreases at higher N-CQDs loading. This modified WO_3 can hinder the charge recombination by providing active sites to facilitate reactions due to lower bandgap energy and PL intensity. The doped N-CQDs increase the trapping sites for the photo-excited electrons and holes, thereby enhance the charge separation and improving the efficiency, which leads to the increased photo-degradation rate of MB (Zheng et al., 2019). It appears to be a threshold level of nitrogen doping level which could have reduced the photocatalyst performance. This can be attributed to the higher degree of photocatalyst agglomeration at higher loadings (Saepurahman et al., 2010) and resulting in higher charge recombination.

The kinetic analysis of MB dye removal using WO_3/N-CQDs samples is performed to evaluate the photocatalytic ability. The MB photodegradation kinetic study is rendered based on two kinetic models, the pseudo-first (Lagergren's rate law) and second order kinetic model. These kinetic models were mostly used for describing the appropriate photocatalytic degradation. The models compare the concentrations of the surface-active site and the pollutants. The pseudo-first and second order kinetic models are expressed in equations (2) and (3) as follows (Abdellah et al., 2018; Visa et al., 2015):

$$\mathrm{Ln}\ \frac{(q_e - q_t)}{q_e} = -K_1 t \tag{2}$$

$$\frac{t}{q_t} = \frac{1}{K_2 q_e^2} + \frac{t}{qe} \tag{3}$$

where t, q_e and q_t are time (min), the amount of pollutants adsorbed at equilibrium and at time t (mg/g), respectively. The K_1 and K_2 represent the pseudo-first order rate constant (min^{-1}), and pseudo-second order rate constant ($min\ g^{-1}\ mg^{-1}$).

Another kinetic model, i.e. the Langmuir-Hinshelwood (L-H) equation, also applied to determine the constant rate removal as comparison. The first-order, and second-order kinetics are expressed in the following equations 5, and 6 (Priya et al., 2019; Wongso et al., 2020).

$$C_t = C_0 e^{-k.t} \tag{4}$$

$$-\ln\left(\frac{C_t}{C_0}\right) = k.t \tag{5}$$

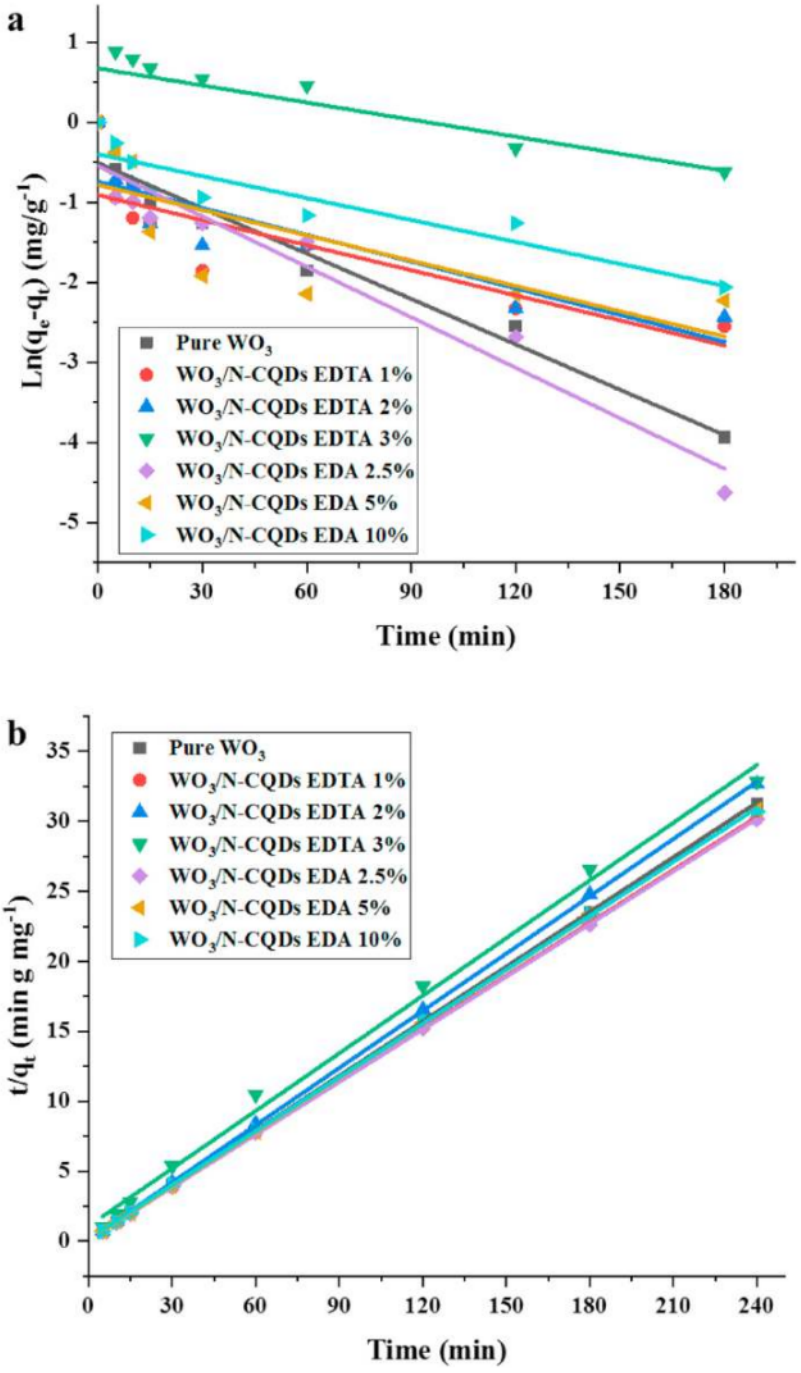

Fig. 10. (a) Pseudo first-order kinetic and (b) Pseudo second-order kinetic of WO_3/N-CQDs.

$$(\frac{1}{C_t}) - (\frac{1}{C_0}) = k.t \quad (6)$$

where C_o is initial MB concentration, C_t is MB concentration at time t and k is removal rate constant (/min). Equation (4) represents the non-linear equation of first-order kinetic. This equation is re-arranged to obtain equation (5), which is in linear form. Moreover, the second-order kinetic also investigated with equation (6).

The data given in Fig. 10 is plotted and fitted with (a) pseudo-

first order as Ln (q_e-q_t) vs. time and (b) pseudo-second order kinetic as t/q_t vs. time, respectively. From both Fig. 10 (a) and (b), the value of removal rate constant and correlation coefficient (R^2) are obtained and listed in Table 3. Besides, first and second-order L-H rate law also applied to compare the fitness of the models. The L-H first and second-order kinetics results listed in Table 4. The results show that the regression coefficient (R^2) of pseudo-second order kinetic is higher than pseudo-first order and L-H models. This suggested that the MB dye removal using WO_3/N-CQDs samples is governed by pseudo-second order kinetic model. The pseudo-second order kinetic model indicates that the WO_3/N-CQDs samples performance are mainly governed by chemisorption on the catalyst surface rather than physisorption for the MB dye removal (Elsayed et al., 2020; Ernawati et al., 2019). The results shown similar trends from previous studies are by using tungsten oxide composite i.e. mesoporous WO_3/TiO_2 nanocomposites (Ernawati et al., 2019), WO_3 – fly ash oxide composite (Visa et al., 2015), hydrogen-treated WO_3 nanofibers (Tahmasebi et al., 2020), and WO_3/sodium alginate/polyvinylpyrrolidone beads (Elsayed et al., 2020) Generally, the composite has increased rate of MB degradation, where WO_3/N-CQDs EDA 2.5% is the best photocatalyst with a removal rate constant of 0.1725 (min g^{-1} mg^{-1}). The result shows a slightly higher k value compared to previous studies of MB removal using mesoporous WO_3/TiO_2 nanocomposites with k at 0.162 min g^{-1} mg^{-1} (Ernawati et al., 2019) and TiO_2/UV system enhanced by air sparging with k value at 0.149 min g^{-1} mg^{-1} (Abdellah et al., 2018).

Moreover, the effect of various initial concentrations of MB is also investigated using the composite in the range of 5–50 ppm. Firstly, the dark experiment was conducted for 50 ppm MB to investigate the composite's adsorption rate at higher MB concentration. The WO_3/N-CQDs EDA 2.5% removed 76.90% MB through adsorption, while the photodegradation has a greater result with 92.93% removal. Subsequently, Fig. 11 (a) depicted the performance of WO_3/N-CQDs EDA 2.5% composite to be slightly decreased from 5 to 50 ppm of MB concentration, with the removal efficiency recorded from 96.86% to 92.93%. The rate of photodegradation for organics is correlated to the active sites and the photo-absorption of the catalyst to produce hydroxyl radicals (Chiou et al., 2008).

Table 3
MB degradation rate constants of WO_3/N-CQDs determined by pseudo first-order and pseudo second-order kinetics.

Samples	Pseudo first-order		Pseudo second-order	
	$k_{1\ abs}$ (min^{-1})	R^2	k_2 (min g^{-1} mg^{-1})	R^2
Pure WO_3	7.875×10^{-5}	0.959	1.416×10^{-1}	0.998
WO_3/N-CQDs EDTA 1%	4.350×10^{-5}	0.700	1.687×10^{-1}	0.993
WO_3/N-CQDs EDTA 2%	4.638×10^{-5}	0.773	0.864×10^{-1}	0.991
WO_3/N-CQDs EDTA 3%	2.967×10^{-5}	0.704	0.173×10^{-1}	0.994
WO_3/N-CQDs EDA 2.5%	8.763×10^{-5}	0.936	1.725×10^{-1}	0.996
WO_3/N-CQDs EDA 5%	4.392×10^{-5}	0.560	1.421×10^{-1}	0.991
WO_3/N-CQDs EDA 10%	3.808×10^{-5}	0.842	1.495×10^{-1}	0.996

Table 4
MB degradation rate constants of WO_3/N-CQDs determined by L-H first-order and second-order kinetics.

Samples	First-order		Second-order	
	k (/min)	R^2	k (/min)	R^2
Pure WO_3	0.00516	0.315	0.00812	0.674
WO_3/N-CQDs EDTA 1%	0.00602	0.288	0.01612	0.726
WO_3/N-CQDs EDTA 2%	0.00362	0.226	0.00378	0.462
WO_3/N-CQDs EDTA 3%	0.00629	0.778	0.00529	0.931
WO_3/N-CQDs EDA 2.5%	0.00682	0.353	0.02017	0.836
WO_3/N-CQDs EDA 5%	0.00558	0.307	0.01009	0.603
WO_3/N-CQDs EDA 10%	0.00671	0.431	0.01207	0.799

Even though higher initial concentrations of MB required more hydroxyl radical, the WO_3/N-CQDs EDA 2.5% composite has adequate active sites to perform photodegradation, though the performance was slightly decreased. Hence, reduce in the rate of photodegradation of the composite was found for higher initial concentrations of MB.

The results from photocatalytic degradation do not indicate the rate of mineralization. Thus, the degree of mineralization was measured using the oxidative mineralization of MB. Table 5 depicted the COD measurement of MB after being treated using WO_3/N-CQDs EDA 2.5% for 5–50 ppm MB concentration. The result shows the composite removes 84.61% of COD at 5 ppm initial concentration after 4 h. At a higher initial concentration, the rate of mineralization is decreased. The COD value decreased from 30 to 6 mg/L, 54 to 13 mg/L and 113 to 31 mg/L for 10, 15 and 50 ppm of MB concentration, respectively. COD removal performance for 50 ppm reaches 72.56%, which indicated that the composite has high photocatalytic activity.

Finally, the stability of the WO_3/N-CQDs EDA 2.5% composite is analyzed by testing the recyclability of the photocatalyst. The 5 ppm of MB is used for each experiment. The photocatalyst was collected from the previous experiment and repeatedly used without any purification. It is shown from Fig. 11 (b) that WO_3/N-CQDs EDA 2.5% has good stability in which the photocatalyst can remove up to 86.85% of MB after the 3rd recycle.

3.9. Proposed mechanism of MB degradation using WO_3/N-CQDs

Fig. 12 demonstrates the proposed mechanism of MB removal using WO_3/N-CQDs. Firstly, the light irradiates the composite to produce electron-holes pair in WO_3 (Eg = 2.175 eV). The excited electrons from valence band were then scavenged by N-CQDs, which reduced the electron-holes recombination (Jamila et al., 2020). Afterward, the electrons react with O_2, producing superoxide radical anion (O_2^-), which in turn generates hydroxide ions (OH^-) and then hydrogen peroxide (H_2O_2) by reacting with water molecules. Conversely, the holes on valence band react with OH^- in water molecules forming •OH radicals. Ultimately, the oxidizing agent and reduction agent formed degrade the MB dyes (Song et al., 2017).

4. Conclusion

In this work, it is reported that N-CQDs alter the bandgap energy, crystallinity, surface area, and photoluminescence properties of the as-prepared WO_3/N-CQDs. Furthermore, the UV–vis spectra exhibit extended and enhanced visible light absorption in the range of 380–700 nm and reduced the bandgap energy up to 1.495 eV. In addition, the photoluminescence intensity of WO_3/N-CQDs was significantly quenched compared to the pristine WO_3. The synthesized WO_3/N-CQDs show increased performance in adsorption and photocatalytic activity with the best performance was obtained from WO_3/N-CQDs EDA 2.5% with an efficiency of 96.86% MB removal, removal rate constant of 0.02017/min and COD removal of 85.61%. Subsequently, the composite shows an excellent result for MB removal at higher concentration, particularly for 50 ppm MB concentration resulting in 92.93% removal efficiency. The composite also exhibits good stability after the 3rd cycle of recyclability test with 86.85% of MB removal. The increasing photocatalytic performance is affected by the lower recombination rate due to photoluminescence's quenching effect and lower bandgap energy, hence resulting in a reduction of charge carrier recombination, which increased the photocatalytic performance of the composites.

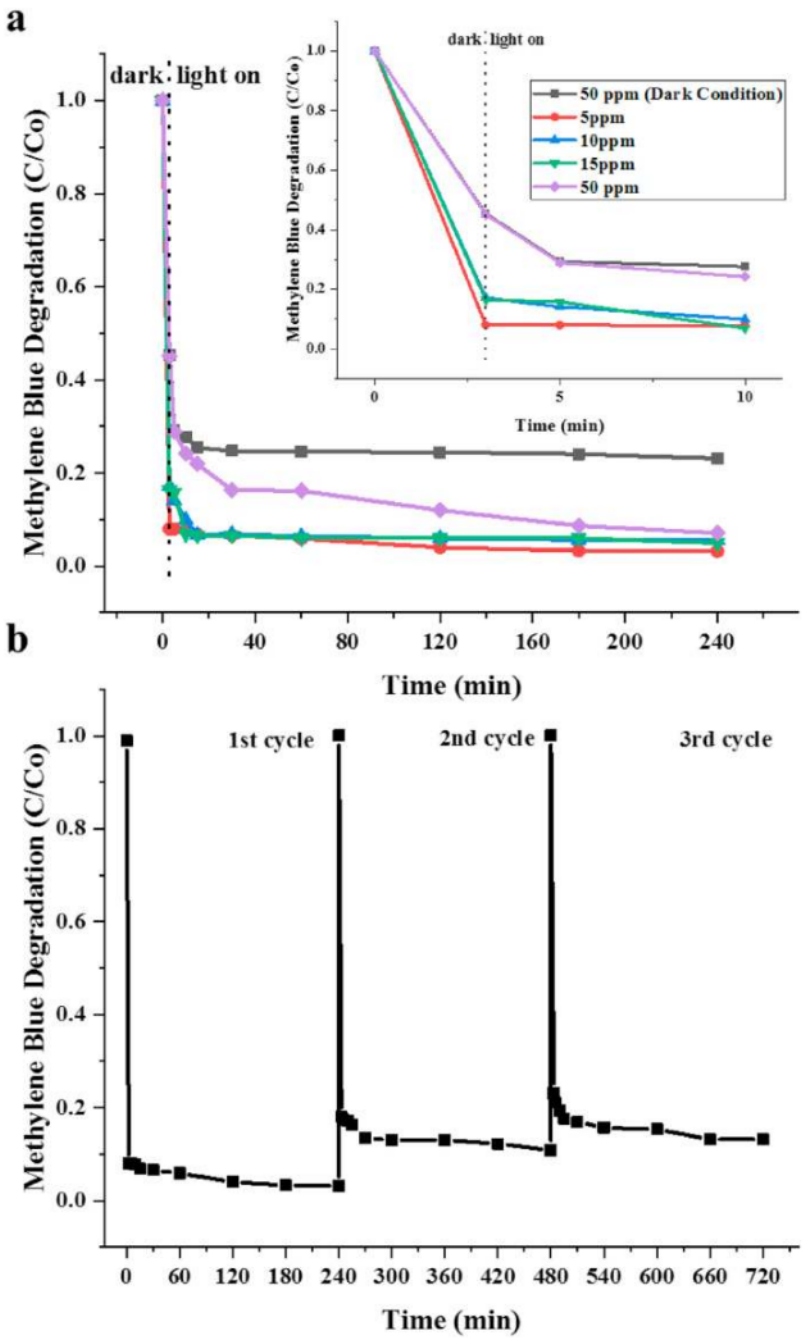

Fig. 11. (a) Photocatalytic performance of WO_3/N-CQDs EDA 2.5% composite at various initial MB concentrations with inset photocatalytic performance at 0–10 min (b) Stability test of WO_3/N-CQDs EDA 2.5% composite.

Credit author statement

Muhammad Wa[46] Nugraha, Methodology, Validation, Investigation, Resources, Writing – original draft, Vis[57]zation, Writing – review & editing. Nur Hafizah Zainal Abidin, Writing – original draft, Resources, Investiga[65], Writing – review & editing. Supandi, Conceptualization, Writing – original draft, Supervision, Writing – [69]view & editing, Project administration. Nonni Soraya Sambudi, Conceptualization, Writing – original draft, Supervision, Writing – review & editing, Funding acquisition, Project

Table 5
COD Measurement of WO_3/N-CQDs EDA 2.5% composite.

MB Concentration (ppm)	COD at 0 min (mg/L)	COD at 240 min (mg/L)	COD Removal Efficiency (%)
5	13	2	84.61
10	30	6	80
15	54	13	75.92
50	113	31	72.56

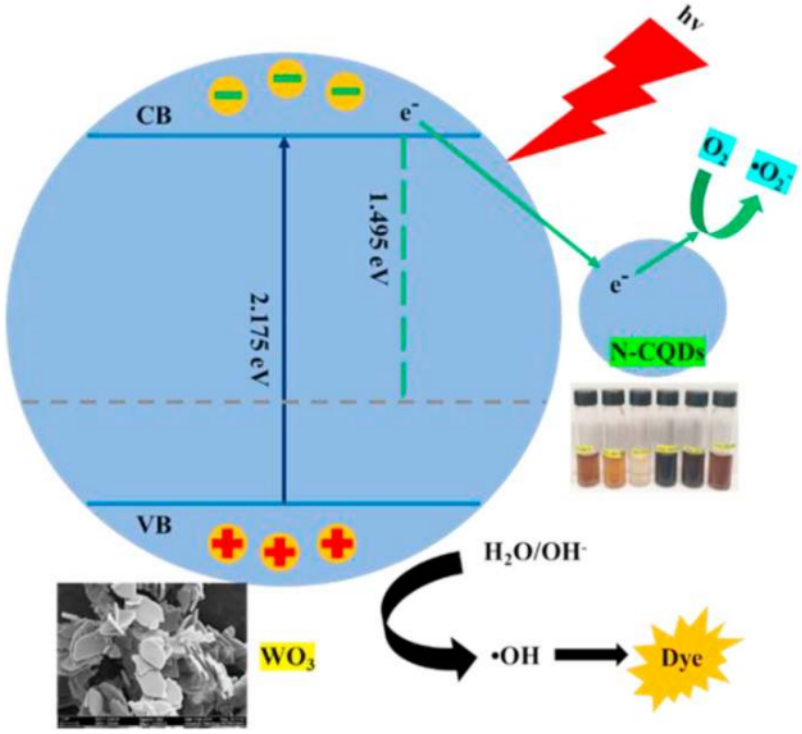

Fig. 12. Proposed mechanism of MB degradation using WO_3/N-CQDs.

administration.

Declaration of competing interest

The authors declare that they have no known competing financial interests or personal relationships that could have appeared to influence the work reported in this paper.

Acknowledgement

The research work was financially supported by YUTP FRG (Yayasan UTP Fundamental Research Grant, YUTP 015LC0-025) and UTP-UHAMKA Collaborative Grant (015ME0-143).

References

Abdellah, M.H., Nosier, S.A., El-Shazly, A.H., Mubarak, A.A., 2018. Photocatalytic decolorization of methylene blue using TiO2/UV system enhanced by air sparging. Alexandria Eng. J. 57, 3727–3735. https://doi.org/10.1016/j.aej.2018.07.018.

Ahmadi, M., Guinel, M.J.F., 2014. Synthesis and characterization of tungstite (WO3·H 2O) nanoleaves and nanoribbons. Acta Mater. 69, 203–209. https://doi.org/10.1016/j.actamat.2014.01.055.

Ahmadi, M., Younesi, R., Guinel, M.J.F., 2014. Synthesis of tungsten oxide nanoparticles using a hydrothermal method at ambient pressure. J. Mater. Res. 29, 1424–1430. https://doi.org/10.1557/jmr.2014.155.

Chandel, A.K., da Silva, S.S., Carvalho, W., Singh, O.V., 2012. Sugarcane bagasse and leaves: foreseeable biomass of biofuel and bio-products. J. Chem. Technol. Biotechnol. 87, 11–20. https://doi.org/10.1002/jctb.2742.

Ching Sim, L., Lin Wong, J., Hong Hak, C., Yan Tai, J., Hon Leong, K., Saravanan, P., Rahman, A., 2018. Sugarcane juice derived carbon dot-graphitic carbon nitride composites for bisphenol A degradation under sunlight irradiation. Beilstein J. Nanotechnol. 9, 353–363. https://doi.org/10.3762/bjnano.9.35.

Chiou, C.H., Wu, C.Y., Juang, R.S., 2008. Influence of operating parameters on photocatalytic degradation of phenol in UV/TiO2 process. Chem. Eng. J. 139, 322–329. https://doi.org/10.1016/j.cej.2007.08.002.

Doma, A.S., Hassan, N., AbdEl-Hamid, A.I., Soliman, H.M.A., 2020. Adsorption of methylene blue dye on hydrothermally prepared tungsten oxide nanosheets. Egypt. J. Chem. 63, 483–498. https://doi.org/10.21608/ejchem.2020.18997.2171.

Elemen, S., Akçakoca Kumbasar, E.P., Yapar, S., 2012. Modeling the adsorption of textile dye on organoclay using an artificial neural network. Dyes Pigments 95, 102–111. https://doi.org/10.1016/j.dyepig.2012.03.001.

Elsayed, E.M., Elnouby, S., M, Gouda, M.H., Elessawy, N.A., Santos, D.M.F., 2020. Effect of the morphology of tungsten oxide embedded in sodium alginate/polyvinylpyrrolidone composite beads on the photocatalytic degradation of methylene blue dye solution. Materials (Basel) 13. https://doi.org/10.3390/ma13081905, 1905.

Ernawati, L., Wahyuono, R.A., Muhammad, A.A., Nurislam Sutanto, A.R., Maharsih, I.K., Widiastuti, N., Widiyandari, H., 2019. Mesoporous WO3/TiO2 nanocomposites photocatalyst for rapid degradation of methylene blue in aqueous medium. Int. J. Eng. Trans. A Basics 32, 1345–1352. https://doi.org/10.5829/ije.2019.32.10a.02.

Gu, W., Yan, Y., Cao, X., Zhang, C., Ding, C., Xian, Y., 2016. A facile and one-step

ethanol-thermal synthesis of MoS2 quantum dots for two-photon fluorescence imaging. J. Mater. Chem. B 4, 27–31. https://doi.org/10.1039/c5tb01839k.
Horiuchi, Y., Toyao, T., Saito, M., Mochizuki, K., Iwata, M., Higashimura, H., Anpo, M., Matsuoka, M., 2012. Visible-light-promoted photocatalytic hydrogen production by using an amino-functionalized Ti(IV) metal-organic framework. J. Phys. Chem. C 116, 20848–20853. https://doi.org/10.1021/jp3046005.
Huang, S., Wang, W., Cheng, J., Zhou, X., Xie, M., Luo, Q., Yang, D., Zhou, Y., Wen, H., Xue, W., 2020. Amino-functional carbon quantum dots as a rational nanosensor for Cu2+. Microchem. J. 159, 105494. https://doi.org/10.1016/j.microc.2020.105494.
Huang, Y.J., Yen, P.J., Wang, H.C., Chen, H.C., Wei, K.H., 2019. An universal electron transport layer involving hydrogen plasma–treated tungsten disulfide nanosheets doped zinc oxide layers for polymer donors with fullerene or small molecule acceptor photovoltaics. Org. Electron. 72, 6–17. https://doi.org/10.1016/j.orgel.2019.05.032.
Jamila, G.S., Sajjad, S., Leghari, S.A.K., Long, M., 2020. Nitrogen doped carbon quantum dots and GO modified WO3 nanosheets combination as an effective visible photo catalyst. J. Hazard Mater. 382, 121087. https://doi.org/10.1016/j.jhazmat.2019.121087.
Lewis, N.S., 2001. Light work with water. Nature 414, 589–590. https://doi.org/10.1038/414589a.
Li, H., Kang, Z., Liu, Y., Lee, S.T., 2012. Carbon nanodots: synthesis, properties and applications. J. Mater. Chem. 22, 24230–24253. https://doi.org/10.1039/c2jm34690g.
Liu, X., Jin, A., Jia, Y., Xia, T., Deng, C., Zhu, M., Chen, C., Chen, X., 2017. Synergy of adsorption and visible-light photocatalytic degradation of methylene blue by a bifunctional Z-scheme heterojunction of WO 3/g-C 3 N 4. Appl. Surf. Sci. 405, 359–371. https://doi.org/10.1016/j.apsusc.2017.02.025.
Liu, X., Pang, J., Xu, F., Zhang, X., 2016. Simple approach to synthesize amino-functionalized carbon dots by carbonization of chitosan. Sci. Rep. 6, 1–8. https://doi.org/10.1038/srep31100.
Liu, X.J., Guo, M.L., Huang, J., Yin, X.Y., 2013. Improved fluorescence of carbon dots prepared from bagasse under alkaline hydrothermal conditions. BioResources 8, 2537–2546. https://doi.org/10.15376/biores.8.2.2537-2546.
Madrakian, T., Maleki, S., Gilak, S., Afkhami, A., 2017. Turn-off fluorescence of amino-functionalized carbon quantum dots as effective fluorescent probes for determination of isotretinoin. Sensor. Actuator. B Chem. 247, 428–435. https://doi.org/10.1016/j.snb.2017.03.071.
Mohammadi, A., Karimi, A.A., 2017. Methylene blue removal using surface-modified TiO 2 nanoparticles: a comparative study on adsorption and photocatalytic degradation. J. Water Environ. Nanotechnol. J. Water Environ. Nanotechnol 2, 118–128. https://doi.org/10.22090/jwent.2017.02.007.
Nogueira, A., Freitas, F.S., Gonçalves, A.S., Morais, A., Benedetti, J.E., 2013. Graphene-like MoS2 as a low-cost counter electrode material for dye-sensitized solar cells. NanoGe J Ener Sust.
Prabhu, S., Nithya, A., Chandra Mohan, S., Jothivenkatachalam, K., 2014. Synthesis, surface acidity and photocatalytic activity of WO3/TiO2 nanocomposites - an overview. Mater. Sci. Forum 781, 63–78. https://doi.org/10.4028/www.scientific.net/MSF.781.63.
Priya, V., Krishna, S.K., Sivakumar, V., Sivakumar, P., 2019. Comparative analysis of photo degradation kinetics using linear and non-linear kinetic models. Rasayan J. Chem. 12, 1360–1368. https://doi.org/10.31788/RJC.2019.1235189.
Saepurahman, Abdullah, M.A., Chong, F.K., 2010. Preparation and characterization of tungsten-loaded titanium dioxide photocatalyst for enhanced dye degradation. J. Hazard Mater. 176, 451–458. https://doi.org/10.1016/j.jhazmat.2009.11.050.
Sayed Abhudhahir, M.H., Kandasamy, J., 2015. Photocatalytic effect of manganese doped WO3 and the effect of dopants on degradation of methylene blue. J. Mater. Sci. Mater. Electron. 26, 8307–8314. https://doi.org/10.1007/s10854-015-3496-z.
Shang, Y., Cheng, X., Shi, R., Ma, Q., Wang, Y., Yang, P., 2020. Synthesis and comparative investigation of adsorption capability and photocatalytic activities of WO3 and W18O49. Mater. Sci. Eng. B Solid-State Mater. Adv. Technol. 262, 114724. https://doi.org/10.1016/j.mseb.2020.114724.
Shi, W., Zhang, X., Brillet, J., Huang, D., Li, M., Wang, M., Shen, Y., 2016. Significant enhancement of the photoelectrochemical activity of WO3 nanoflakes by carbon quantum dots decoration. Carbon N. Y. 105, 387–393. https://doi.org/10.1016/j.carbon.2016.04.051.
Sial, Q.A., Javed, M.S., Lee, Y.J., Duy, L.T., Seo, H., 2020. Flexible and transparent graphene-based supercapacitors decorated with nanohybrid of tungsten oxide nanoflakes and nitrogen-doped-graphene quantum dots. Ceram. Int. 46, 23145–23154. https://doi.org/10.1016/j.ceramint.2020.06.094.
Song, B., Wang, T., Sun, H., Shao, Q., Zhao, J., Song, K., Hao, L., Wang, L., Guo, Z., 2017. Two-step hydrothermally synthesized carbon nanodots/WO3 photocatalysts with enhanced photocatalytic performance. Dalton Trans. 46, 15769–15777. https://doi.org/10.1039/c7dt03003g.
Su, L., Fang, J., Lu, Z., 1997. Photochromic and photoelectrochemical behavior of thin semiconductor WO3 films. Mater. Chem. Phys. 51, 85–87. https://doi.org/10.1016/S0254-0584(97)80272-6.
Tahmasebi, N., Sezari, S., Zaman, P., 2020. Fabrication and characterization of hydrogen-treated tungsten oxide nanofibers for cationic dyes removal from water. Solid State Sci. 100, 106073. https://doi.org/10.1016/j.solidstatesciences.2019.106073.
Tetsuka, H., Asahi, R., Nagoya, A., Okamoto, K., Tajima, I., Ohta, R., Okamoto, A., 2012. Optically tunable amino-functionalized graphene quantum dots. Adv. Mater. 24, 5333–5338. https://doi.org/10.1002/adma.201201930.
Tian, J., Leng, Y., Zhao, Z., Xia, Y., Sang, Y., Hao, P., Zhan, J., Li, M., Liu, H., 2015. Carbon quantum dots/hydrogenated TiO2 nanobelt heterostructures and their broad spectrum photocatalytic properties under UV, visible, and near-infrared irradiation. Nanomater. Energy 11, 419–427. https://doi.org/10.1016/j.nanoen.2014.10.025.
Ţucureanu, V., Matei, A., Avram, A.M., 2016. FTIR spectroscopy for carbon family study. Crit. Rev. Anal. Chem. https://doi.org/10.1080/10408347.2016.1157013.
Visa, M., Bogatu, C., Duta, A., 2015. Tungsten oxide - fly ash oxide composites in adsorption and photocatalysis. J. Hazard Mater. 289, 244–256. https://doi.org/10.1016/j.jhazmat.2015.01.053.
Wang, H., Yuan, X., Wu, Y., Zeng, G., Chen, X., Leng, L., Wu, Z., Jiang, L., Li, H., 2015. Facile synthesis of amino-functionalized titanium metal-organic frameworks and their superior visible-light photocatalytic activity for Cr(VI) reduction. J. Hazard Mater. 286, 187–194. https://doi.org/10.1016/j.jhazmat.2014.11.039.
Wongso, V., Sambudi, N.S., Sufian, S., Isnaeni, 2020. The effect of hydrothermal conditions on photoluminescence properties of rice husk-derived silica-carbon quantum dots for methylene blue degradation. Biomass Convers. Biorefinery 1–14. https://doi.org/10.1007/s13399-020-00662-9.
Wu, M., Wang, Y., Wu, W., Hu, C., Wang, X., Zheng, J., Li, Z., Jiang, B., Qiu, J., 2014. Preparation of functionalized water-soluble photoluminescent carbon quantum dots from petroleum coke. Carbon N. Y. 78, 480–489. https://doi.org/10.1016/j.carbon.2014.07.029.
Xin, B., Wang, P., Ding, D., Liu, J., Ren, Z., Fu, H., 2008. Effect of surface species on Cu-TiO 2 photocatalytic activity. Appl. Surf. Sci. 254, 2569–2574. https://doi.org/10.1016/j.apsusc.2007.09.002.
Yahya, M.A., Al-Qodah, Z., Ngah, C.W.Z., 2015. Agricultural bio-waste materials as potential sustainable precursors used for activated carbon production: a review. Renew. Sustain. Energy Rev. https://doi.org/10.1016/j.rser.2015.02.051.
Yan, F., Kong, D., Fu, Y., Ye, Q., Wang, Y., Chen, L., 2016. Construction of carbon nanodots/tungsten trioxide and their visible-light sensitive photocatalytic activity. J. Colloid Interface Sci. 466, 268–274. https://doi.org/10.1016/j.jcis.2015.12.043.
Zangeneh, H., Zinatizadeh, A.A.L., Habibi, M., Akia, M., Hasnain Isa, M., 2015. Photocatalytic oxidation of organic dyes and pollutants in wastewater using different modified titanium dioxides: a comparative review. J. Ind. Eng. Chem. https://doi.org/10.1016/j.jiec.2014.10.043.
Zhan, Y., Liu, Y., Liu, Q., Liu, Z., Yang, H., Lei, B., Zhuang, J., Hu, C., 2018. Size-controlled synthesis of fluorescent tungsten oxide quantum dots via one-pot ethanol-thermal strategy for ferric ions detection and bioimaging. Sensor. Actuator. B Chem. 255, 290–298. https://doi.org/10.1016/j.snb.2017.08.043.
Zhang, J., Liu, J., Wang, X., Mai, J., Zhao, W., Ding, Z., Fang, Y., 2019. Construction of Z-scheme tungsten trioxide nanosheets-nitrogen-doped carbon dots composites for the enhanced photothermal synergistic catalytic oxidation of cyclohexane. Appl. Catal. B Environ. 259, 118063. https://doi.org/10.1016/j.apcatb.2019.118063.
Zhang, J., Yao, T., Guan, C., Zhang, N., Zhang, H., Zhang, X., Wu, J., 2017. One-pot preparation of ternary reduced graphene oxide nanosheets/Fe2O3/polypyrrole hydrogels as efficient Fenton catalysts. J. Colloid Interface Sci. 505, 130–138. https://doi.org/10.1016/j.jcis.2017.05.101.
Zhang, J., Zhang, X., Dong, Shanshan, Zhou, X., Dong, Shuangshi, 2016. N-doped carbon quantum dots/TiO2 hybrid composites with enhanced visible light driven photocatalytic activity toward dye wastewater degradation and mechanism insight. J. Photochem. Photobiol. A Chem. 325, 104–110. https://doi.org/10.1016/j.jphotochem.2016.04.012.
Zheng, G., Wang, J., Liu, H., Murugadoss, V., Zu, G., Che, H., Lai, C., Li, H., Ding, T., Gao, Q., Guo, Z., 2019. Tungsten oxide nanostructures and nanocomposites for photoelectrochemical water splitting. Nanoscale 11, 18968–18994. https://doi.org/10.1039/c9nr03474a.

Synthesis of tungsten oxide/ amino-functionalized sugarcane bagasse derived-carbon quantum dots (WO3/N-CQDs) composites for methylene blue removal

ORIGINALITY REPORT

17%	8%	15%	4%
SIMILARITY INDEX	INTERNET SOURCES	PUBLICATIONS	STUDENT PAPERS

PRIMARY SOURCES

1	Zhang, Jun, Xueying Zhang, Shanshan Dong, Xian Zhou, and Shuangshi Dong. "N-doped carbon quantum dots/TiO2 hybrid composites with enhanced visible light driven photocatalytic activity toward dye wastewater degradation and mechanism insight", Journal of Photochemistry and Photobiology A Chemistry, 2016. Publication	1%
2	ugspace.ug.edu.gh Internet Source	1%
3	onlinelibrary.wiley.com Internet Source	1%
4	allie.dbcls.jp Internet Source	1%
5	Saepurahman, M.A. Abdullah, F.K. Chong. "Preparation and characterization of tungsten-loaded titanium dioxide	1%

photocatalyst for enhanced dye degradation", Journal of Hazardous Materials, 2010
Publication

6	www.hindawi.com Internet Source	1 %
7	Saepurahman, M.A. Abdullah, F.K. Chong. "Dual-effects of adsorption and photodegradation of methylene blue by tungsten-loaded titanium dioxide", Chemical Engineering Journal, 2010 Publication	<1 %
8	Submitted to Universiti Malaysia Pahang Student Paper	<1 %
9	Guangwei Zheng, Jinshu Wang, Hu Liu, Vignesh Murugadoss et al. "Tungsten oxide nanostructures and nanocomposites for photoelectrochemical water splitting", Nanoscale, 2019 Publication	<1 %
10	"Environmental Remediation Through Carbon Based Nano Composites", Springer Science and Business Media LLC, 2021 Publication	<1 %
11	Jun Di, Jiexiang Xia, Mengxia Ji, Bin Wang, Xiaowei Li, Qi Zhang, Zhigang Chen, Huaming Li. "Nitrogen-Doped Carbon Quantum Dots/BiOBr Ultrathin Nanosheets: In Situ	<1 %

	Strong Coupling and Improved Molecular Oxygen Activation Ability under Visible Light Irradiation", ACS Sustainable Chemistry & Engineering, 2015 Publication	
12	L. D. Kasmiarno, D. Floresyona, R. Raissa, N. S. Pambudi. " Synthesis of TiO /GO nanocomposite for Methylene Blue Degradation ", IOP Conference Series: Materials Science and Engineering, 2020 Publication	<1 %
13	d-nb.info Internet Source	<1 %
14	pure.iiasa.ac.at Internet Source	<1 %
15	www.frontiersin.org Internet Source	<1 %
16	Manoj Pudukudy, Qingming Jia. "Facile chemical synthesis of nanosheets self-assembled hierarchical H2WO4 microspheres and their morphology-controlled thermal decomposition into WO3 microspheres", Journal of Materials Science, 2019 Publication	<1 %
17	Melvin Ng Hau Kwan, C.P. Leo, S.M.N. Arosa Senanayake, G.K. Lim, M.K. Tan. "Carbon-dot dispersal in PVA thin film for food colorant	<1 %

	sensing", Journal of Environmental Chemical Engineering, 2019 Publication	
18	Anna Kubacka, Marcos Fernández-García, Gerardo Colón. "Advanced Nanoarchitectures for Solar Photocatalytic Applications", Chemical Reviews, 2011 Publication	<1 %
19	Wu, Mingbo, Yue Wang, Wenting Wu, Chao Hu, Xiuna Wang, Jingtang Zheng, Zhongtao Li, Bo Jiang, and Jieshan Qiu. "Preparation of functionalized water-soluble photoluminescent carbon quantum dots from petroleum coke", Carbon, 2014. Publication	<1 %
20	doaj.org Internet Source	<1 %
21	Submitted to Chulalongkorn University Student Paper	<1 %
22	Sonica Sondhi. "Sustainable approaches in effluent treatment", Elsevier BV, 2020 Publication	<1 %
23	Submitted to University of Edinburgh Student Paper	<1 %
24	Submitted to University of Leeds Student Paper	<1 %

25	Yu Horiuchi, Takashi Toyao, Masakazu Saito, Katsunori Mochizuki et al. "Visible-Light-Promoted Photocatalytic Hydrogen Production by Using an Amino-Functionalized Ti(IV) Metal–Organic Framework", The Journal of Physical Chemistry C, 2012 Publication	<1 %
26	Submitted to Alexandru Ioan Cuza University of Iasi Student Paper	<1 %
27	Majid Ahmadi, Maxime J.-F. Guinel. "Synthesis and characterization of tungstite (WO3·H2O) nanoleaves and nanoribbons", Acta Materialia, 2014 Publication	<1 %
28	Md Moniruddin, Ellis Oppong, David Stewart, Christopher McCleese, Ajit Roy, Juliusz Warzywoda, Nurxat Nuraje. " Designing CdS-Based Ternary Heterostructures Consisting of Co-Metal and CoO Cocatalysts for Photocatalytic H Evolution under Visible Light ", Inorganic Chemistry, 2019 Publication	<1 %
29	Qadeer Akbar Sial, Ranveer Singh, Le Thai Duy, Shahid Iqbal, Il-Han Yoo, Shankara S. Kalanur, Hyungtak Seo. "Nitrogen-doped carbon dot anchored 1-D WO3 for enhanced solar water splitting: A nano surface imaging	<1 %

evidence of charge separation and accumulation", International Journal of Hydrogen Energy, 2021
Publication

30	etd.lib.nsysu.edu.tw Internet Source	<1 %
31	repository.elizadeuniversity.edu.ng Internet Source	<1 %
32	Ali Aghamali, Morteza Khosravi, Hamed Hamishehkar, Nasser Modirshahla, Mohammad A. Behnajady. "Preparation of novel high performance recoverable and natural sunlight-driven nanocomposite photocatalyst of Fe3O4/C/TiO2/N-CQDs", Materials Science in Semiconductor Processing, 2018 Publication	<1 %
33	www.e-sciencecentral.org Internet Source	<1 %
34	www.researchsquare.com Internet Source	<1 %
35	Ailing Jin, Yushuai Jia, Changfeng Chen, Xin Liu, Junzhe Jiang, Xiangshu Chen, Fei Zhang. "Efficient Photocatalytic Hydrogen Evolution on Band Structure Tuned Polytriazine/Heptazine Based Carbon Nitride Heterojunctions with Ordered Needle-like	<1 %

Morphology Achieved by an In Situ Molten Salt Method", The Journal of Physical Chemistry C, 2017
Publication

36	Gen Li, Feng Wang, Peng Liu, Zheming Chen, Ping Lei, Zhongshan Xu, Zengxi Li, Yanfen Ding, Shimin Zhang, Mingshu Yang. "Polymer dots grafted TiO 2 nanohybrids as high performance visible light photocatalysts", Chemosphere, 2018 Publication	<1 %
37	iopscience.iop.org Internet Source	<1 %
38	Akrami, Ahmad, and Ali Niazi. "Synthesis of maghemite nanoparticles and its application for removal of Titan yellow from aqueous solutions using full factorial design", Desalination and Water Treatment, 2016. Publication	<1 %
39	Lam, Sze-Mun, Jin-Chung Sin, Ahmad Zuhairi Abdullah, and Abdul Rahman Mohamed. "ZnO nanorods surface-decorated by WO3 nanoparticles for photocatalytic degradation of endocrine disruptors under a compact fluorescent lamp", Ceramics International, 2012. Publication	<1 %

40	Qiuhong Bai, Huimin Li, Luwei Zhang, Cong Li, Yehua Shen, Hiroshi Uyama. "Flexible Solid-State Supercapacitors Derived from Biomass Konjac/Polyacrylonitrile-Based Nitrogen-Doped Porous Carbon", ACS Applied Materials & Interfaces, 2020 Publication	<1 %
41	purehost.bath.ac.uk Internet Source	<1 %
42	Dongfang Wang, Guilong Zhang, Zhangyu Dai, Linglin Zhou, Po Bian, Kang Zheng, Zhengyan Wu, Dongqing Cai. "Sandwich-like Nanosystem for Simultaneous Removal of Cr(VI) and Cd(II) from Water and Soil", ACS Applied Materials & Interfaces, 2018 Publication	<1 %
43	Jun Di, Jiexiang Xia, Xiaoliu Chen, Mengxia Ji, Sheng Yin, Qi Zhang, Huaming Li. "Tunable oxygen activation induced by oxygen defects in nitrogen doped carbon quantum dots for sustainable boosting photocatalysis", Carbon, 2017 Publication	<1 %
44	M.H. Abdellah, S.A. Nosier, A.H. El-Shazly, A.A. Mubarak. "Photocatalytic decolorization of methylene blue using TiO2/UV system enhanced by air sparging", Alexandria Engineering Journal, 2018	<1 %

Publication

45	Peyman Gholami, Alireza Khataee, Amit Bhatnagar. "Photocatalytic degradation of antibiotic and hydrogen production using diatom-templated 3D WO3-x@mesoporous carbon nanohybrid under visible light irradiation", Journal of Cleaner Production, 2020 Publication	<1 %
46	Submitted to University of Nebraska, Lincoln Student Paper	<1 %
47	Yuefang Hu, Zhenming Chen, Feiyan Lai, Jinfang Li. "Biomass-codoped carbon dots: efficient fluorescent probes for isocarbophos ultrasensitive detection and for living cells dual-color imaging", Journal of Materials Science, 2019 Publication	<1 %
48	Zhenting Yuan, Huoshuai Huang, Najun Li, Dongyun Chen, Qingfeng Xu, Hua Li, Jinghui He, Jianmei Lu. "All-solid-state WO3/TQDs/In2S3 Z-scheme heterojunctions bridged by Ti3C2 quantum dots for efficient removal of hexavalent chromium and bisphenol A", Journal of Hazardous Materials, 2021 Publication	<1 %

core.ac.uk

49	Internet Source	<1%
50	dokumen.pub Internet Source	<1%
51	repository.ubn.ru.nl Internet Source	<1%
52	www.jstage.jst.go.jp Internet Source	<1%
53	www.science.gov Internet Source	<1%
54	Fang Chen, Hongwei Huang, Chao Zeng, Xin Du, Yihe Zhang. " Achieving Enhanced UV and Visible Light Photocatalytic Activity for Ternary Ag/AgBr/BiOIO : Decomposition for Diverse Industrial Contaminants with Distinct Mechanisms and Complete Mineralization Ability ", ACS Sustainable Chemistry & Engineering, 2017 Publication	<1%
55	Gancheng Zuo, Yuting Wang, Wei Liang Teo, Qiming Xian, Yanli Zhao. "Direct Z-scheme TiO2–ZnIn2S4 nanoflowers for cocatalyst-free photocatalytic water splitting", Applied Catalysis B: Environmental, 2021 Publication	<1%

56	Houjuan Qi, Min Teng, Miao Liu, Shouxin Liu et al. "Biomass-derived nitrogen-doped carbon quantum dots: highly selective fluorescent probe for detecting Fe3+ ions and tetracyclines", Journal of Colloid and Interface Science, 2019 Publication	<1 %
57	Laleh Mahmoudi, Sara Asadi, Zahra Al-Mousavi, Ramin Niknam. "A randomized controlled clinical trial comparing calcitriol versus cholecalciferol supplementation to reduce insulin resistance in patients with non-alcoholic fatty liver disease", Clinical Nutrition, 2020 Publication	<1 %
58	Md Rifat Hasan, Nepu Saha, Thomas Quaid, M. Toufiq Reza. "Formation of Carbon Quantum Dots via Hydrothermal Carbonization: Investigate the Effect of Precursors", Energies, 2021 Publication	<1 %
59	Nur Aqilah Mohd Razali, Wan Norharyati Wan Salleh, Farhana Aziz, Lau Woei Jye, Norhaniza Yusof, Ahmad Fauzi Ismail. "Review on tungsten trioxide as a photocatalysts for degradation of recalcitrant pollutants", Journal of Cleaner Production, 2021 Publication	<1 %

60 Qadeer Akbar Sial, Muhammad Sufyan Javed, Young-Jae Lee, Le Thai Duy, Hyungtak Seo. "Flexible and transparent graphene-based supercapacitors decorated with nanohybrid of tungsten oxide nanoflakes and nitrogen-doped-graphene quantum dots", Ceramics International, 2020 <1%
Publication

61 Quan Li, Zhiwei Guo, Xiaoyan Zhao, Taoyi Zhang, Jing Chen, Yun Wei. "One-pot synthesis of 2,2'-dipicolylamine derived highly photoluminescent nitrogen-doped carbon quantum dots for Fe3+ detection and fingermark identification", Nanotechnology, 2020 <1%
Publication

62 Rab Nawaz, Chong Fai Kait, Ho Yeek Chia, Mohamed Hasnain Isa, Lim Wen Huei, Nurul Tasnim Sahrin, Nasrullah Khan. "Countering major challenges confronting photocatalytic technology for the remediation of treated palm oil mill effluent: A review", Environmental Technology & Innovation, 2021 <1%
Publication

63 Wei Gu, Xueyu Pei, Yuxiao Cheng, Cuiling Zhang, Jidong Zhang, Yinghan Yan, Caiping Ding, Yuezhong Xian. "Black Phosphorus Quantum Dots as the Ratiometric <1%

Fluorescence Probe for Trace Mercury Ion Detection Based on Inner Filter Effect", ACS Sensors, 2017
Publication

64	Yingke Zhu, Hao Yao, Pingkai Jiang, Jiandong Wu, Xi Zhu, Xingyi Huang. "Two-Dimensional High-k Nanosheets for Dielectric Polymer Nanocomposites with Ultrahigh Discharged Energy Density", The Journal of Physical Chemistry C, 2018 Publication	<1 %
65	dspace.vutbr.cz Internet Source	<1 %
66	eprints.utar.edu.my Internet Source	<1 %
67	erepository.uoeld.ac.ke Internet Source	<1 %
68	István Székely, Monica Baia, Klára Magyari, Bíborka Boga, Zsolt Pap. "The effect of the pH adjustment upon the WO3-WO3·0.33H2O-TiO2 ternary composite systems' photocatalytic activity", Applied Surface Science, 2019 Publication	<1 %
69	Matulonis, Ursula A., Philipp Harter, Charlie Gourley, Michael Friedlander, Ignace Vergote, Gordon Rustin, Clare Scott, Werner Meier,	<1 %

Ronnie Shapira-Frommer, Tamar Safra, Daniela Matei, Anitra Fielding, Stuart Spencer, David Parry, Lynda Grinsted, and Jonathan A. Ledermann. "Olaparib maintenance therapy in patients with platinum-sensitive, relapsed serous ovarian cancer and a BRCA mutation: Overall survival adjusted for postprogression poly(adenosine diphosphate ribose) polymerase inhibitor therapy : Olaparib Therapy: Adjusted OS", Cancer, 2016.
Publication

---

70 Xin Liu, Changfeng Chen, Hongwu Ye, Yushuai Jia, Yiyun Wu, Ailing Jin, Yabin Wang, Xiangshu Chen. "One-step hydrothermal growth of carbon nanofibers and insitu assembly of Ag nanowire@carbon nanofiber@Ag nanoparticles ternary composites for efficient photocatalytic removal of organic pollutants", Carbon, 2018 <1 %
Publication

---

71 Chunzhen Yang, Ming Zhou, Ming Zhang, Liang Gao. "Mitigating the Degradation of Carbon-Supported Pt Electrocatalysts by Tungsten Oxide Nanoplates", Electrochimica Acta, 2016 <1 %
Publication

---

72 Wee-Jun Ong, Lling-Lling Tan, Yun Hau Ng, Siek-Ting Yong, Siang-Piao Chai. " Graphitic <1 %

Carbon Nitride (g-C N)-Based Photocatalysts for Artificial Photosynthesis and Environmental Remediation: Are We a Step Closer To Achieving Sustainability? ", Chemical Reviews, 2016

Publication

Exclude quotes	Off	Exclude matches	Off
Exclude bibliography	On		